POLITECNICO DI TORINO

Master's Degree in Biomedical Engineering

Master's Degree Thesis

Body Composition Estimation from 3-Dimensional Optical Scans Using Principal Component Analysis in Youth Soccer Players

Supervisors

Prof. Ing. Kristen Mariko MEIBURGER

Prof. Ing. Alberto BOTTER

Prof. Marco Alessandro MINETTO

Ing. Marta BOCCARDO

Candidate

Alessandro GARAU

July 2025

A nonna,
che stai guardando da lassù,
questo traguardo lo dedico a te.

Abstract

This thesis aims to predict total and regional body composition derived from dual-energy X-ray absorptiometry (DXA) using principal component analysis (PCA) on raw and digitally reposed three-dimensional optical (3DO) whole-body scans in youth soccer players. This work is motivated by the growing demand for safe, accessible, and low cost methods of assessing body composition, since the current gold standard, DXA, is often impractical due to cost, exposure to ionizing radiation, and limited accessibility, particularly in youth sports. The purpose of this study is to evaluate the feasibility and accuracy of this approach to determine whether it can serve as a valid and reliable tool for monitoring body composition. A total of 429 participants, including 270 males and 159 females between 14 and 23 years old, took part in the study. The acquisition campaign included body weight and height measurements, one whole-body DXA scan, and two 3DO scans acquired via Mobile Fit app. Two different analyses were carried out on the avatars: A-pose and T-pose. The raw A-pose avatars were used as provided by the Mobile Fit app, without any processing. The T-pose avatars, on the other hand, were sent to Meshcapade to be digitally reposed to a standardized pose. PCA was applied to perform dimensionality reduction and capture complex shape features. The algorithm was independently applied to male and female avatars. The datasets, which included principal components (PCs), anthropometric variables, and DXA outcomes, were randomly split into training (80%) and test (20%) sets. Stepwise linear regression was used to construct prediction models for DXA body composition outcomes. The performance of the models was evaluated using fivefold cross-validation applied to the training set. The results showed that estimates of total and regional lean mass were highly accurate in male soccer players, with coefficients of determination (R^2) above 0.82 for hybrid models that combine PCs and digital anthropometry, and up to 0.92 for total lean mass. In contrast, fat mass estimates were inaccurate since they reported R^2 values close to or below 0. In female soccer players, none of the models achieved high performance in total and regional lean mass estimates (R^2 as high as 0.62 for total lean mass), and fat mass predictions achieved moderate accuracy (R^2 as high as 0.4 for body fat percentage). This study demonstrated that accurate predictions were reached for specific outcomes and subgroups, suggesting that the homogeneity in body shape and composition among young athletes may limit the ability of PCA to capture body shape variance. In this context, models that relied only on digital anthropometric measurements performed as well as, or better, than those that used PCs.

Acknowledgements

Alla fine di questo percorso, ci tengo a ringraziare tutti coloro che sono stati parte integrante della mia vita, sin dal principio che in questi anni. Come molti di voi già sanno, non sono molto bravo a dimostrare la mia gratitudine e l'affetto alle persone, ma sappiate che a tutti voi va il mio più sentito grazie.

In primis, ci tengo a ringraziare con tutto me stesso Mamma e Papà, che hanno sempre sostenuto le mie scelte, mi hanno incoraggiato a seguire la mia strada e mi hanno insegnato a non arrendermi mai, neanche nei momenti più difficili. Un grazie non sarà mai abbastanza per avermi permesso di vivere questa esperienza, senza alcuna preoccupazione se non quella di costruire il mio futuro come meglio credo.

Un pensiero affettuoso va a Nonna, che è stata sempre presente durante questo percorso e ha gioito con me a ogni traguardo raggiunto, spesso anche più di me. Avrei voluto tanto condividere con te anche questo momento, ma so che sei e sarai sempre con me.

Agli Zii e alle Cugine, per tutti i momenti passati assieme, tutte le volte che siete venuti a trovarmi e tutte le sciate in montagna.

Agli amici di sempre, che, anche se non ho potuto frequentare come un tempo, sono rimasti sempre vicini e presenti, anche quando sparivo per lunghi periodi. Sapere di poter contare sempre su di voi, sia quando sono in Sardegna che quando sono a Torino, è stato fondamentale.

Infine, un ringraziamento va a tutti i colleghi diventati amici, al gruppo del CX e in maniera speciale a tutti gli amici sardi che ho rincontrato e conosciuto qua, alla forte amicizia che è nata e al sentirmi sempre a casa quando siamo assieme. Siete arrivati nella mia vita in un periodo difficile, e non potevo sperare in un momento migliore per incontrarvi. Avete reso questi anni, sia dentro che fuori l'università, più leggeri e indimenticabili. Vi porterò sempre con me.

Table of Contents

List of Tables

List of Figures

Acronyms

BMI
Body Mass Index

MRI
Magnetic Resonance Imaging

CT
Computed Tomography

DXA
Dual-Energy X-ray Absorptiometry

ADP
Air Displacement Plethysmography

BIA
Bioelectrical Impedance Analysis

BMC
Bone Mineral Content

3DO
Three-Dimensional Optical

LASS
Loughborough Anthropometric Shadow Scanner

ToF
Time-of-Flight

RGB

Red-Green-Blue

PCA

Principal Component Analysis

PC

Principal Component

BF

Body Fat

MSI

Muscle-to-Stomach Index

ALM

Appendicular Lean Mass

SVD

Singular Value Decomposition

NaN

Not a Number

BIC

Bayesian Information Criterion

R^2

Coefficient of Determination

RMSE

Root Mean Square Error

Chapter 1

Introduction

1.1 Body Composition and Anthropometric Analysis

As defined by Messiah [1], body composition refers to the proportion of fat, muscle, and bone in a person's body. It is most often expressed as a percentage of body fat or lean body mass, or as a lean-to-fat mass ratio. Lean mass includes muscle, bone, skin, internal organs, and body water, whereas fat mass consists primarily of subcutaneous fat and visceral adipose tissue. Closely related to body composition is anthropometry, the study of physical measurements of the human body. Common anthropometric variables, including height, weight, lengths, skinfold thickness, and circumferences, have proven useful for investigating patients with endocrine and metabolic disorders [2].

Accurate assessments of total and regional body composition are essential for monitoring physical activity and dietary interventions [3]. They also play a central role in diagnosing and managing a wide range of medical conditions, such as obesity, type 2 diabetes, cardiovascular diseases, metabolic syndrome, malnutrition, sarcopenia, and cancer [4, 5, 6, 7, 8, 9]. Body composition assessments are not limited to pathological contexts. They are widely used in sports and rehabilitation medicine to support personalized training and recovery protocols [2], and are considered a key component in weight management programs for children and adolescents, contributing to the prevention of future cardiovascular and metabolic diseases [10, 11, 12]. Anthropometric measurements are commonly used in athletic populations to optimize performance and reduce the risk of injury [13].

Notably, regional body composition indicators often demonstrate greater predictive power than whole-body metrics. For instance, trunk fat is linked to insulin resistance and dyslipidemia; the trunk-to-leg volume ratio is associated with diabetes and mortality; and the appendicular lean mass index is connected

to sarcopenia [3, 14, 15]. The body mass index (BMI), which expresses body weight relative to height, is commonly used as an indirect indicator of body fatness and is strongly associated with various metabolic risk factors [16]. While higher BMI values are generally linked to increased diseases risk among normal weight and overweight adults [17], this metric presents a significant limitation: it cannot distinguish between fat and fat-free mass, both of which play an important role in disease risk [18]. Consequently, more specific anthropometric and regional body composition measurements, such as waist circumference, waist-to-hip ratio, and visceral adipose tissue, have proven to be more effective indicators of metabolic diseases and mortality risk than BMI [19, 20, 21].

For many years, researchers and clinicians have estimated body fat mass and fat-free mass using a variety of manual anthropometric measurements. However, accurate results from traditional manual anthropometric assessment require trained operators and are limited to linear and circumferential measures, failing to capture detailed aspects of a subject's shape [22]. Additionally, these measurements are less reliable in overweight people and may be socially or culturally unacceptable [3].

A variety of imaging and non-imaging techniques can be used to assess body composition. Advanced imaging modalities, such as magnetic resonance imaging (MRI) and computed tomography (CT), provide highly accurate assessments of regional body composition [23]. However, these techniques are expensive and require specialized equipment and trained personnel. In the case of CT, exposure to ionizing radiation limits their routine and repeated use, particularly in pediatric populations and non clinical settings. This is especially problematic in pediatric research because people undergo the most significant changes in body mass and composition between the ages of 5 and 18 [24].

Over the years, more accessible methods have been developed, including dual-energy X-ray absorptiometry (DXA), air displacement plethysmography (ADP), and bioelectrical impedance analysis (BIA). Each method has specific advantages and limitations. DXA is widely regarded as the clinical gold standard in body composition assessment [25]. It provides accurate estimates of whole-body and regional fat and lean mass, but it involves ionizing radiation and requires trained technicians [26]. The Medical and Scientific Commission of International Olympic Committee and the International Society for Clinical Densitometry caution against more than two scans per year for children and four per year for adults, due to the cumulative radiation dose [27]. ADP is non-invasive and relatively accurate for measuring whole-body composition. However, it lacks compartmental resolution and is sensitive to subject cooperation and environmental conditions [28]. BIA is inexpensive and easy to administer, making it suitable for field and clinical use. However, its accuracy is influenced by hydration status, and it relies on population specific calibration models [29].

Despite their widespread adoption, these methods present challenges related

to cost, accessibility, and technical requirements. An ideal method would include total and regional body composition, and automated anthropometry. It should be low cost, require little to no training to operate, be free of ionizing radiation, and produce results that are accurate and relevant to metabolic risk [30, 31].

Consequently, there is a growing interest in alternative approaches, such as three-dimensional optical (3DO) imaging, which has recently emerged as a versatile and promising tool for assessing body composition and health. 3DO scanners produce detailed surface renderings of the body in under a minute, and the instrument's software automatically generates circumference and length measurements across the entire body, data that would otherwise require significantly more time and effort to obtain through manual technique [10].

1.2 Dual-Energy X-ray Absorptiometry

Given its established role as the clinical gold standard for body composition assessment, a comprehensive understanding of the physical principles underlying dual-energy X-ray absorptiometry (DXA, Figure 1.1) is essential. The following section provides a detailed overview of the physical concepts of DXA, based on the review by Pietrobelli at al. [32].

Photon Sources and Detectors

DXA operates according to the principles of photon absorptiometry, which requires the use of both a photon source and a detector. A significant advancement in photon absorptiometry has been the adoption of X-ray sources. X-rays are

Figure 1.1: Example of Lunar iDXA scanner (GE Healthcare, Chicago, IL, USA), from [33].

produced when fast-moving electrons are suddenly decelerated by the tungsten or tungsten alloy anode inside a vacuum tube. X-rays consist of a broad spectrum of photon energies, which typically range from 15 keV to 80 keV. For DXA applications it is necessary to create two main energy peaks within the spectrum. To achieve this, a "K-edge" filter, which is commonly made of a rare-earth material such as cerium (Ce) or samarium (Sm), is placed in the path of the X-ray beam. These filters selectively attenuate photons with energies slightly above the K-shell binding energy of the filter material. Another approach to generating dual-energy X-ray spectra is to pulse the kV of the X-ray tube between sequential measurement points. After passing through the subject, X-ray photons are quantified using either photomultiplier tubes with sodium iodide scintillators or electronic detectors. A specific energy "window" or range is defined for each of DXA's two main energies, so that only photons falling within the selected windows are counted as belonging to one of the two beams. Regarding the source of X-ray emission, there has been a technological evolution with the transition from pencil-beam densitometers to fan-beam densitometers, as reported by Messina et al. [34]. Pencil-beam densitometers emit a single, highly collimated, rectilinear beam of X-rays coupled with a single detector. Fan-beam technology, in contrast, uses a fan-shaped beam coupled with multiple detectors, allowing for shorter scan times and better image resolutions.

Attenuation Phenomenon

The fundamental process underlying DXA measurements is the attenuation of X-ray photons as they traverse body tissues. As photons pass through the subject's tissues, their intensity decreases due to two main physical interactions: the Compton scattering and photoelectric effect. These interactions result in the absorption or scattering of photons, reducing the number that reach the detector. For monoenergetic photons passing through a homogeneous absorber (an element, chemical compound or solution), the attenuation of beam intensity follows an exponential law (equation (1.1)). The reduction in transmitted intensity (I) relative to the initial intensity (I_0) is proportional to the substance's linear attenuation coefficient (μ) and the path length (L) that the photons travel:

$$I = I_0 e^{-\mu \times L} \tag{1.1}$$

Since the linear attenuation coefficient (μ) depends on density (ρ), it is convenient to calculate the mass attenuation coefficient (μ_m) as μ/ρ, when working with tissues of different densities. This makes it possible to compare the attenuation properties of different tissues, regardless of their physical density.

For heterogeneous absorbers, such as human soft tissues, the transmitted photon intensity is related to the fractional mass of the substance, as indicated by the following equation:

$$I = I_0 e^{\sum(-f_i \times \mu_{mi} \times M)} \tag{1.2}$$

where f_i and μ_{mi} are respectively the mass fraction and the mass attenuation coefficient of the i-th component as heterogeneous absorber, and M is the absorber mass. The basic photon intensity equations can be expressed as I/I_0. Generally, attenuation decreases as photon energy increases, and substances with higher mass attenuation coefficients exhibit greater attenuation. The mass attenuation coefficient of an element is constant at any given photon energy, and it is known from experimental measurements.

Ratio Value and Component Identification

After passing through the body, the intensities of the low energy (L) and high energy (H) X-ray beams are measured. The ratio (R) of these two transmitted intensities, as reported in equation (1.3), provides important information about tissue composition.

$$R = ln(I/I_0)_L / ln(I/I_0)_H \tag{1.3}$$

In the case of a heterogeneous absorber, the ratio R depends on both the mass attenuation coefficient and the mass fraction of each component. In contrast, for a homogeneous absorber, R is simply the ratio of the component's mass attenuation coefficient at the two energies.

DXA produces the R value, which can be used to identify unknown components. Each element has a specific and known R value at the specified energies. In a two-component mixture, the measured R value and the known mass attenuation coefficients of the components at the two energies can be used to calculate the mass fraction of each component. Thus, a dual-energy system can be used to estimate the fractional masses of two-component mixtures. The human body can be assumed to be either "bone mineral plus soft tissue" or "fat plus bone mineral-free lean". For a heterogeneous absorber, since $f_1 + f_2 = 1$, the R value can be approximated as:

$$R = f_1 \times R_1 + f_2 \times R_2 \tag{1.4}$$

then

$$f_1 = (R - R_2)/(R_1 - R_2) \tag{1.5}$$

and

$$f_2 = (R_1 - R)/(R_1 - R_2) \tag{1.6}$$

The DXA approach for body composition analysis is based on the assumption that the human body consist of three components: fat, bone mineral, and lean soft tissue (Figure 1.2), each of which has unique X-ray attenuation properties. In theory, distinguishing three unknown components requires measurements at three different photon energies; however, DXA systems operate using only two energies. Consequently, they can only resolve the fractional masses of a two-component mixture.

In the DXA method, the first step for calculating the three components is to divide pixels into two categories: soft tissue plus bone mineral, and soft tissue only (fat and lean). The first step in pixel separation, also known as "point typing", is determining the R value for each pixel in a total body DXA scan. Pixels containing bone have higher composite R values because the R value for bone mineral is significantly higher than that of soft tissue. To differentiate pixels containing bone mineral from those made entirely of soft tissue, an R value threshold must be specified.

Equations (1.5) and (1.6) can be used to evaluate the fat and lean composition of soft tissue pixels. Lean soft tissue and fat samples, as well as other materials used as calibration standards, are measured in order to determine the constants $R1$ and $R2$ in these equations. Estimating the soft tissue composition of pixels containing bone is difficult and requires certain assumptions. The first and most straightforward approach was to assume that the soft tissue composition over

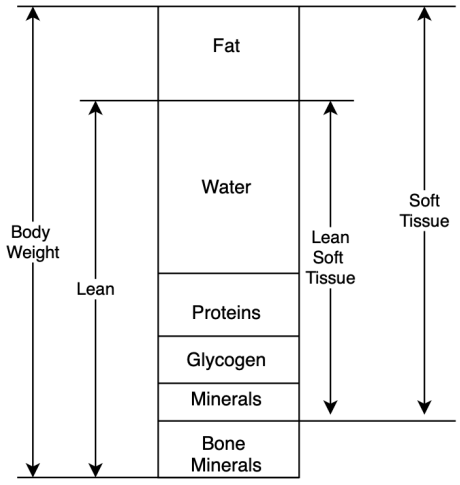

Figure 1.2: Schematic representation of body composition compartments as assessed by DXA, showing the relationships between body weight, fat mass, lean soft tissue, and bone mineral content. Image taken from Pietrobelli et al. [32].

bone was comparable to the average of all the surrounding soft tissue. The soft tissue distribution, however, clearly deviates from uniformity; the body's surface has a higher proportion of adipose tissue. Near appendicular bones there is more lean muscle, especially skeletal muscle. Thus, measured X-ray attenuation, the three assumed component R values, image processing techniques, and soft tissue distribution models can all be used to quantify the fat, lean soft tissue, and bone mineral content (BMC) of every pixel in the scan image.

1.3 Three-Dimensional Optical Imaging

Although DXA offers exact and consistent body composition measurements, its clinical use is still limited by elements including exposure to ionizing radiation, cost, and the necessity of qualified personnel, as previously mentioned. These limitations have generated interest in alternative approaches. Among these, three-dimensional optical (3DO) imaging has recently emerged as a versatile and promising technology. The following section reviews 3DO imaging systems, paying particular attention to the technological concepts that support their operation and use in body composition measurement.

Historical Background and Development

As reported by Heymsfield et al.[35], in the mid-nineteen eighties, Loughborough University in England received a request from a textile manufacturer searching for detailed human shape data to optimize garment production. The company's goal was to create a "non-contact machine that is reasonably transportable and sufficiently speedy in operation to survey economically a large sample of the British population." This initiative resulted in the creation of the Loughborough Anthropometric Shadow Scanner (LASS) in 1987. It was a device that integrated a television camera, a projector, and a 360° rotating table on which participants stood during measurement. The introduction of the LASS marked the birth of the field of automated anthropometry. Over the following decades, rapid technological advancements have led to increasingly sophisticated methods of quantifying human body shape. These methods include laser and structured light systems, millimeter wave radar, and multi-view camera approaches [35].

1.3.1 Three-Dimensional Scanning Technologies

Three commonly used scanning technologies are employed for acquiring human body data: passive stereo, structured light, and time-of-flight (ToF) imaging. The technological principles underlying these modalities are described in this section according to Bartol et al. [36].

Passive Stereo and Photogrammetry

Passive stereo is a measurement technique used for 3D reconstruction from several camera views. The study of measuring items using photos is called photogrammetry. In the context of 3D scanning, the terms passive stereo and photogrammetry are occasionally used interchangeably. RGB cameras are used to capture color images, and it is assumed that multiple cameras point toward the subject.

The most basic passive stereo setup is a binocular stereo, which consists of two RGB cameras oriented either horizontally or vertically. The triangulation and correspondences discovered in the photos serve as the foundation for the reconstruction. As seen in Figure 1.3, the point P in the 3D scene projects to pixel p_1 in the first image and p_2 in the second image. Nevertheless, the matching pixel location p_2 for a specified pixel location p_1 is unknown beforehand. By comparing an image block surrounding p_1 with the most similar block along the epipolar line l, one can find the point p_2. The depth of a point P is triangulated using the disparity, or difference between the associated pixel coordinates. By utilizing multi-view-stereo techniques or pairing couples of cameras, the stereo approach can be expanded to include more than two cameras.

Another stereo reconstruction approach is the monocular moving-camera-based 3D reconstruction, in which every frame is regarded as a distinct camera. The general monocular techniques estimate camera locations in each frame and recreate a 3D scene together. In order to identify correspondences, the images' keypoints are first identified and compared. After that, the correspondences are used to estimate the camera parameters and do preliminary 3D reconstruction. Since camera locations can be determined before reconstruction, human 3D scanning is typically simple. This is done so that the person is either standing on a revolving

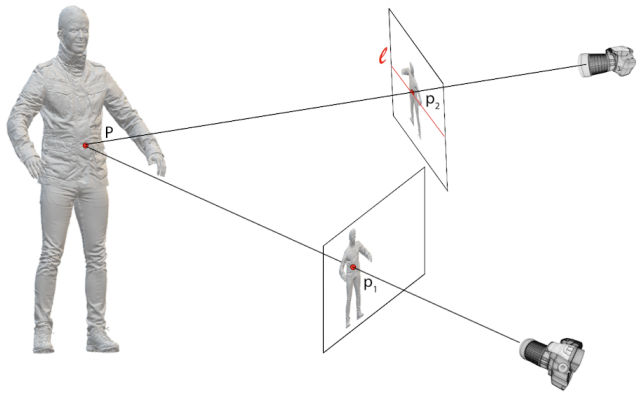

Figure 1.3: Passive stereo approach. Image taken from Bartol et al. [36].

platform that simulates camera rotation, or the camera is rotating around the person. The stereo reconstruction principles explained above can be applied to obtain a dense 3D reconstruction.

Structured Light

The usual approach to improve the poor 3D reconstruction quality of passive stereo in cases of low or repeating texture is to project a textured pattern onto the scene. Active stereo enhances passive stereo by improving the correspondence search between views by projecting a pattern of light onto the body. In contrast, structured light techniques look for correspondences between the camera and the light pattern.

Two scanner types are distinguished based on structured light technology: laser and projector scanners. A laser is used to generate dot or stripe patterns onto the scene in laser scanners, as shown in Figure 1.4. Compared to projector-based scanners, laser scanners offer sub-millimeter accuracy and a more straightforward decoding process. However, because the laser line must sweep the entire body, laser scanners often have a slow scanning time.

Since they can project more complex 2D patterns and scan the entire body at once from a single perspective, projector-based scanners (Figure 1.5) are typically faster than laser scanners. The number of projected patterns (single or multi-shot), color (achromatic or colored), transitions (continuous or discrete), or structured form (stripes, grids, dot arrays, gradients, etc.) are some of the general classifications of projected light patterns that have been proposed. Short-duration achromatic

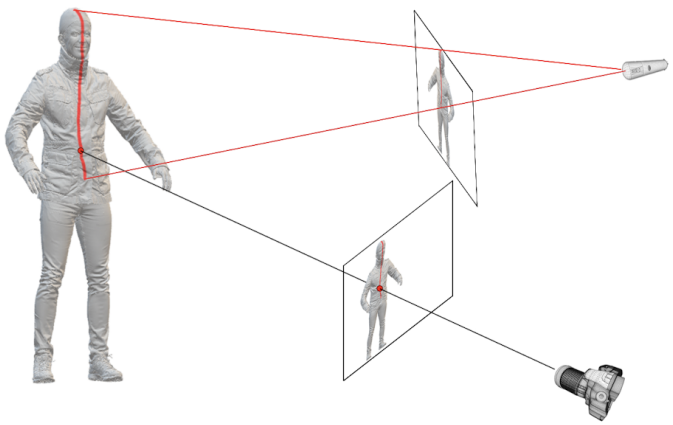

Figure 1.4: Laser-based structured light approach. Image taken from Bartol et al. [36].

multi-shot patterns are typically employed for quasi-static human 3D scanning, because they offer a trade-off between reconstruction accuracy and acquisition speed.

Camera-to-light-source correspondences are determined based on the projected light and pattern. In order to identify the light projections in the image, laser-based methods primarily use pattern detection algorithms. On the other hand, visible-light scanners have more complex pattern decoding systems. Ray-to-ray or ray-to-plane triangulation can be used to recreate the 3D human body once the correspondences have been acquired.

Time-of-Flight

Time-of-flight scanners, illustrated in Figure 1.6, calculate the time it takes for an emitted light signal to travel from the source to the 3D scene and back to the sensor. The information regarding the distance is proportional to the time of flight of the light signal.

The light emitter and the photodetector are the two main primary components of a ToF scanner. The light emitter sends a modulated beam of light, usually in the near-infrared spectrum, using a laser or an LED. The light from the emitter is dispersed throughout the scene via the lens. Typically, a matrix of point-wise sensors is used by the photodetector.

There are two types of reconstruction techniques: continuous-wave (indirect) and pulsed-light (direct). Continuous-wave techniques gather the signal's time-dependent intensity data and indirectly assess the round-trip time of a light pulse

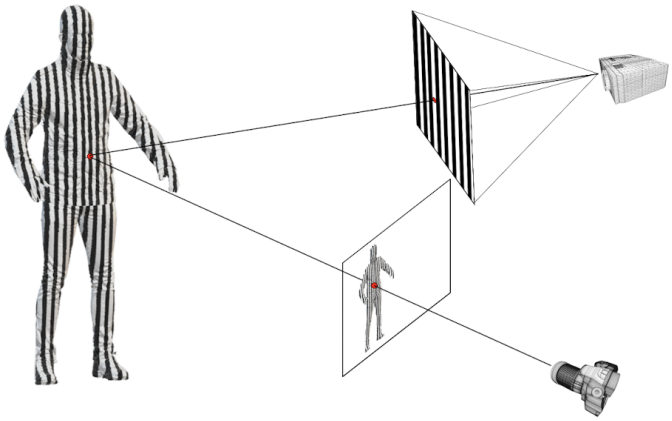

Figure 1.5: Projector-based structured light approach. Image taken from Bartol et al. [36].

that is released. The cross-correlation of the emitted and the received light signals is then used to determine the distance of a point from their phase shift. Pulsed-light techniques use time-to-digital or time-to-amplitude circuits to directly calculate the round-trip duration of a light pulse that is emitted.

Low scanning resolution is the main issue with single ToF camera scanners, despite the fact that they offer low-cost, small, accurate, and reliable sensors with reduced power consumption. As a result, ToF remains less applicable for body measurement and quasi-static scanning.

Structured light is the preferred technique since it provides the highest accuracy and resolution. This is also confirmed by the number of commercial devices that use structured light scanners, as will be demonstrated later. Table 1.1 compares the main technical characteristics of passive stereo, structured light, and ToF methods, highlighting the key differences in methodology, performance, and sources of error.

Table 1.1: Main characteristics of the three 3D scanning technologies with respect to human body scanning, from Bartol et al. [36].

	Passive stereo	**Structured light**	**Time-of-flight**
Method	triangulation	triangulation	time-to-distance conversion
Illumination	passive (ambient)	active (visible, IR)	
Scanning range	several meters	$<$ 5 m (illumination source limited)	
Dynamic scanning	yes	yes (slower movement only)	yes
Accuracy range	mm – cm	μm – cm	mm – cm
Resolution range	mm	μm – mm	mm
Main issues	textureless body parts	light interference	lower resolution, multi-camera interference

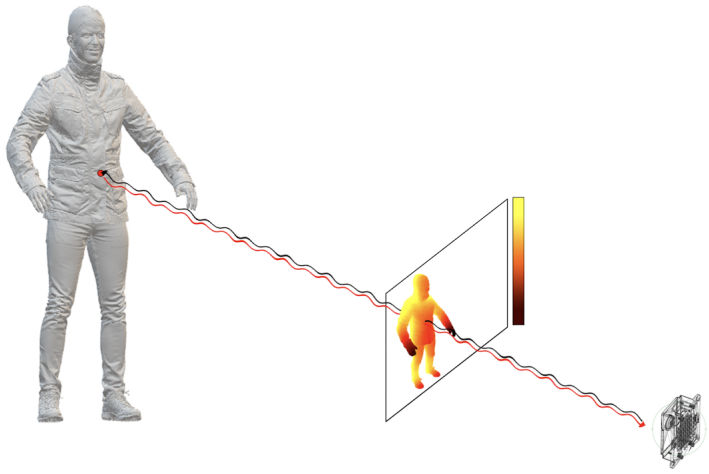

Figure 1.6: Time-of-flight approach. Image taken from Bartol et al. [36].

1.3.2 Data Acquisition and Processing

The procedure for obtaining anthropometric measurements from three-dimensional optical (3DO) imaging systems can be organized into a series of steps, as shown in Figure 1.7. The technical overview presented in this section is based on the frameworks described by Bartol et al. [36] and Heymsfield et al. [35]. Acquisition and processing are the two primary stages of this pipeline. During the acquisition stage, raw data are collected from the subject in the form of 3D point clouds, depth maps, or 2D RGB images, depending on the specific scanning technology. The processing stage comprise the following steps: feature extraction, model fitting, and measurement extraction. First, the obtained data is used to identify relevant features, such as body silhouettes and anatomical keypoints. Based on the features or raw image data the optimal human 3D template mesh is estimated. Finally, the fitted model is used to compute anthropometric measurements.

Scanning

The human body may be measured in motion or in a stationary posture, with regard to the acquisition protocol when employing 3D scanners. In static scanning, the subject is instructed to assume a specific position and remain still until the scan is complete. Longer acquisition times for 3D scanners can cause people to unintentionally move during acquisition, which introduces inaccuracies. In these cases, it is possible to classify the scanning as quasi-static. The results of scanning

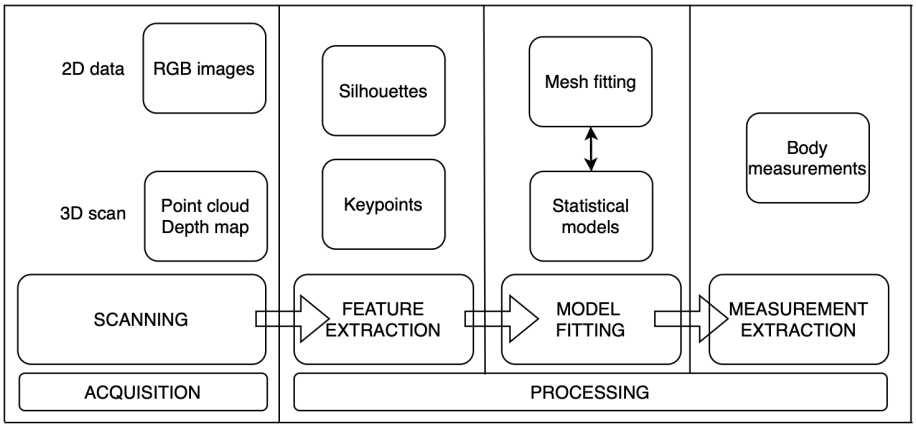

Figure 1.7: Schematic representation of the data acquisition and processing pipeline in a three-dimensional optical (3DO) imaging system, adapted from Bartol et al. [36] and Heymsfield et al. [35].

are usually a 3D point cloud, depth maps, or 2D RGB images.

Feature Extraction

Keypoints and silhouettes are two types of features typically derived from 3D scans and images. Keypoints locations can either be automatically predicted from a 3D scan or based on markers. A chosen subset of human joints is often represented by the keypoints. The entire human body or specific body parts may be represented by silhouettes, which are 3D points or pixels.

Model Fitting

Model fitting is a set of techniques used to find the 3D template mesh that best represents the given input. The input can be a silhouette, 2D or 3D keypoints, or a 3D scan. In the context of body measurement estimation, template meshes have the advantage of having a fixed number of vertices and matching vertices with same semantics for all registered meshes in the dataset. Body measurements can be obtained for each mesh in the same way after they have been obtained for a single mesh. There are two main model fitting techniques: mesh fitting (registration or deformation) and mesh regression using statistical models.

Measurement Extraction

After creating a 3D mesh, an anatomical meaning must be assigned to the mesh surface in order to measure volumes, widths, circumferences, and linear dimensions. Every scanner have its own proprietary body measurement software; however, the underlying concepts of measuring are similar. Major joints and limbs are recognized as landmarks and they are used to define different body regions. After that, the body point cloud or mesh is sliced along a number of planes, usually orthogonal to a limb or parallel to the floor. Body circumferences and/or contour lengths are measured using convex hull or comparable techniques. Originally, 3D body scan measurements technologies were created for use in the military or in industry for tailored clothing applications. Therefore, the commonly defined measurements are similar to those a tailor would take (neck, arm, and torso circumferences, seat depth and width, etc.). Within a body region, specific measurements are established in relation to recognized landmarks.

1.3.3 Technical Limitations

The main technical limitations of the current 3D scanning technologies are discussed in this section, based on the thorough review by Heymsfield et al. [35].

Hardware

3DO scanners use cameras to collect data from multiple perspectives of the body. Either several cameras placed around the body, or a system that rotates the camera or the subject being scanned are needed for the hardware. Systems with multiple cameras tend to be larger and more expensive than those with a single camera. For this reason, systems designed by several companies include a platform that rotates the subject 360°. For children or the elderly, who could find it difficult to maintain a fixed position during the scan's rotation phase, this design could be problematic. Handlebars are incorporated into the rotating systems base to limit movement, however the handles are included in the final 3D image, which may induce artifacts when estimating certain surface measurements.

Landmarking

There are clear and consistent disparities between 3DO and standard technique measurements, which are probably caused by differences in cutoff points and landmarking. Due to these discrepancies, 3DO data cannot be directly compared to large preexisting datasets from various scanning systems. The crotch and armpits are typically simple to spot on an avatar, and segmenting body parts can start there. However, landmark detection can be especially difficult on scans of individuals with high BMI, as the crotch, armpits, and bony landmarks may be covered by a lot of soft tissue.

Avatar Repair

In areas that are occluded or difficult to see, such as the top of the head, under the arms, or between the legs, the 3D scan and its rebuilt geometry frequently contain holes or gaps. The precision of anthropometric measurements could be impacted by these data gaps. Consequently, 3D scan repair is required, particularly in cases when the missing areas are substantial. Currently, commercial 3D modeling software or general context-insensitive hole-filling algorithms are frequently used to merely remedy avatar defects.

1.3.4 Commercial Devices

As highlighted by Bullas et al. [37], 3DO imaging technology used to be expensive and difficult to access outside of specialized research environments. However, in recent years, growing interest and applications in fields such as entertainment, fashion, ergonomics, and healthcare have driven market expansion, resulting in lower costs and improved accessibility. There are now a wide range of commercial

3DO imaging systems available (Figure 1.8), each with different combinations of hardware, software, calibration techniques, anthropometric definitions, and data acquisition procedures. Consequently, the degree of validity and accuracy in body composition estimation can vary significantly between systems.

The main user and system details of four commercially available 3DO imaging systems are reported in Table 1.2. It also provides details about their reported accuracy of the mesh, anthropometric measurements, and body composition estimates. This table, adapted from Bullas et al. [37], emphasizes the variety of available solutions and the differences in device performance.

Mobile Fit

In this study, the 3DO scans were acquired using the Mobile Fit solution (Size Stream LLC, Cary, NC, USA), consisting of a mobile application for iOS and Android devices, user registration platform and scanning technology, an Apple iPad with Wi-Fi, and a mounting stand [39]. The scan takes less than 30 seconds and provides over 240 body measurements and health metrics [39]. The application uses artificial intelligence and machine learning algorithms to create a 3D humanoid avatar of the subject from two photographs (one frontal and one lateral), with all processing performed locally on the device [40, 41, 13]. Currently, no technical details regarding the image processing pipeline or the proprietary algorithms implemented by Mobile Fit have been publicly disclosed. Details about the acquisition protocol adopted in this study are reported in Section 2.1.

Figure 1.8: Example of Fit3D Proscanner (Fit3D Inc., Redwood City, CA, USA), from [38].

Table 1.2: Main characteristics and body composition estimation details of commercially available 3DO imaging systems, in which "-" stands for not reported, adapted from Bullas et al. [37].

System Name	**Fit3D Proscanner**	**Naked**	**Shapescale**	**Styku S100X**
Manufacturer	Fit3D	Naked Labs	Shapescale	Styku
Manufacturer location	USA	USA	USA	USA
System description	Rotating platform and instrumented tower	Rotating platform and instrumented mirror	Rotating instrumented tower	Rotating platform
Technology	Structured light	Structured light	Structured light	Structured light
Hardware cost (USD)	$10,000	$1395	$799	$4950
Subscription cost (annual)	No subscription costs	No subscription costs	$9.99/$12.99	£799
System volume (w x d x h (cm))	91.44 x 182.88 x 180.34	76.5 x 90.5 x 158.8	120 x 120 x 145	131 x 185 x 117
User mass min./max. (kg)	-/272	-/150	11.3/160	23/250
User height min./max. (cm)	-/213	100/198	-/193	137/194
Min. age (years)	13+	18+	2+	18+
Capture duration (s)	35	15	<60	30-40
Reported accuracy of mesh (+/- mm/%)	-	∼2.5/-	∼1.6/1.5	-
Reported accuracy of anthropometrics (+/- mm/%)	-	∼5-15/-	-	∼2.5-5/0.5
Body composition components estimated	Fat Mass (kg, %); Lean Mass (kg, %)	Fat Mass (kg, %); Lean Mass (kg, %)	Fat Mass (%: absolute, regional); Lean Mass (%: absolute, regional)	Fat Mass (kg, %); Lean Mass (kg, %)
Body comp. estimation algorithm	Proprietary algorithm	Proprietary algorithm	-	Proprietary algorithm
How body comp. estimate algorithm were created	DXA and anthropometry	DXA and anthropometry	-	Advanced: DXA and anthropometry; Basic: BIA and anthropometry
Reported accuracy of body comp. estimates (±kg/%)	-/∼5	-/2.5	-	-
How was accuracy of body comp. estimates established	DXA and anthropometry	-	-	-

1.4 Estimation of Body Composition through 3DO Imaging

The development of 3DO imaging systems has led to their increased use in clinical and research settings, emerging as a promising tool for assessing body composition. While the previous section provided a detailed explanation of the technology behind 3DO imaging, this section focuses on clinical applications, specifically body composition estimation. Table 1.3 offers a comparison of the key technological advantages and limitations of 3DO imaging with those of DXA, which continues to be the clinical gold standard. The comparison shows that 3DO imaging has several advantages, including the absence of ionizing radiation, portability, and automation. However, it also has limitations that must be considered in a clinical setting. In addition to body composition estimation, 3DO imaging systems have a number of other biomedical and clinical applications, as shown in Figure 1.9. These applications include anthropometric measurements, prediction of health risks, energy expenditure, DXA or MRI images, as well as body shape analysis. The rest of this section will focus on the use of 3DO imaging for the estimation of body composition.

The first studies investigating the use of 3DO imaging systems for body composition estimation focused on extracting automated anthropometric measurements (e.g., circumferences, lengths, and volumes) from 3DO scans and applying regression models to predict total and regional body composition variables derived from DXA.

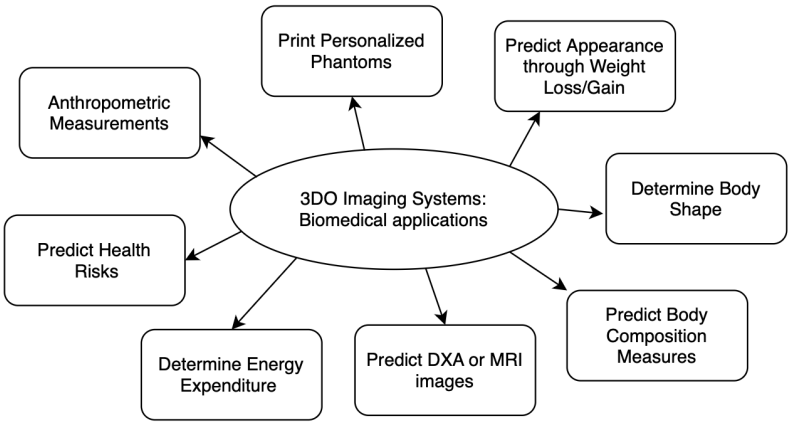

Figure 1.9: Main biomedical applications of 3DO imaging systems, adapted from Heymsfield et al. [35].

Table 1.3: Main technological and practical advantages and limitations of DXA and 3DO imaging for body composition assessment.

	DXA	**3DO Imaging**
Radiation	Uses ionizing radiation, not suitable for frequent use or pregnancy	None, safe for all ages and frequent use
Accessibility	Hospital/clinic only	Portable, suitable for non-clinical use
Operation	Requires trained technicians	Simple, minimal training required
Scan speed	5-15 min per scan	<1 min per scan
Output	Gold standard for fat, lean, and bone mass	3D avatar, anthropometric measurements, indirect fat/lean estimates
Repeatability	Limited by radiation	Unlimited scans, ideal for follow-up
Cost	High purchase and maintenance costs	Lower purchase and running costs
Automation	Partially automated	Highly automated, some devices are self-service
Limitations	Radiation, cost, accessibility, technical requirements, pediatric/adolescent use	Sensitive to movement, system variability

Ng et al. [42] were among the first to validate the use of digital anthropometry obtained from whole-body 3DO scans, acquired on a Fit3D Proscanner (Fit3D Inc., Redwood City, CA, USA), for estimating body composition in adults. In their study, the researchers used automatically extracted anthropometric measurements as predictors in multiple linear regression models. These models achieved high correlation and low prediction errors compared to DXA. Subsequent studies have extended this approach to different population and devices. For example, Wong et al. [10] evaluated the performance of the Fit3D Proscanner in children and adolescents. They demonstrated that body composition estimates derived from linear regression models based on digital anthropometry were highly correlated with DXA measurements for percent body fat, fat mass, and fat-free mass. Their study demonstrated the feasibility and accuracy of body composition assessment using 3DO imaging systems in the pediatric population. Bennett et al. [3] confirmed the

validity and repeatability of total and regional body composition estimates in a large adult sample by using a different commercial device, the Styku S100 (Styku LLC, Los Angeles, CA). Together, these studies established automated digital anthropometry from 3DO imaging systems as a practical and reliable alternative for assessing body composition.

Recent studies have progressed beyond traditional regression models based on digital anthropometry, using machine learning and advanced statistical shape modeling approaches to increase prediction accuracy of body composition from 3DO scans. Lu et al. [43] estimated body fat percentage using a machine learning framework. They integrated shape descriptors into a single prediction model and obtained high accuracy.

The Shape Up! studies have established a substantial scientific foundation for these approaches by using large samples of 3D body scans from adult and pediatric populations. Standardizing 3D meshes to a common template and using principal component analysis (PCA), a dimensionality reduction method, that capture complex shape features outside of conventional anthropometric measurements form the fundamental approach. These principal components (PCs) are then used as predictors in linear regression models to estimate DXA total and regional body composition. Ng et al. [22] first demonstrated the accuracy of using body shape descriptors (PCs), while Sobhiyeh et al. [44] automated this PCA-based approach. Tian et al. [45, 24] developed device-agnostic models and extended these methods to pediatric populations. These studies showed that a single statistical shape model could be applied across scanning devices by registering meshes from different 3DO imaging systems into fixed topology meshes with anatomical consistency, preserving accuracy and precision in body composition estimates. Wong et al. [30, 31] have digitally registered and reposed 3DO meshes to a standardized T-pose using Meshcapade (Meshcapade GmbH, Tübingen, Germany). The majority of pose-related variance was eliminated by reposing the meshes to a standardized pose, leaving mostly shape variance. Pose variance was eliminated to produce more precise and accurate models, which could lead to improved body composition monitoring. In summary, statistical shape modeling using PCA on standardized 3D meshes, combined with automated, device-agnostic, and pose-independent pipelines, now represents the state of the art for estimating body composition from whole-body 3DO scans. These innovations form the scientific basis for the methodology adopted in this thesis.

1.5 Thesis Outline

The aim of this study is to predict total and regional body composition derived from DXA in youth soccer players using statistical shape modeling (PCA) applied

to raw and digitally reposed 3DO whole-body scans. The 3DO scans were acquired using the Mobile Fit app, which generates a 3D avatar from two photographs of each subject. The rationale behind this thesis is an increasing demand for safe, accessible, and low cost methods to assess body composition in young athletes, since the current gold standard (DXA) is impractical due to cost, limited accessibility, and exposure to ionizing radiation. This study seeks to assess the feasibility and accuracy of this approach in a youth sports setting to determine whether it can be used as a valid and reliable method to monitor body composition. If successful, this methodology could provide coaches, clinicians, and researchers with a rapid, non-invasive, and portable tool for tracking physical development, optimizing training and nutritional programs, and identifying medical problems in young athletes.

The thesis is structured as follows:

- **Chapter 1** provides an overview of the thesis topic and states the aim of the study. It also discusses the physical and technological concepts of DXA and 3DO imaging systems, as well as the use of 3DO imaging for body composition estimation.
- **Chapter 2** describes the acquisition protocol, the data used, and the methodology adopted in this study.
- **Chapter 3** presents the results obtained from the analyses.
- **Chapter 4** discusses the results.
- **Chapter 5** provides conclusions and suggestions for future developments.

Chapter 2

Materials and Methods

The methodology presented in this study was developed in collaboration with the Department of Surgical Sciences, Division of Physical Medicine and Rehabilitation at Molinette Hospital in Turin.

2.1 Participants and Protocol

The study participants are 270 young male soccer players and 159 young female soccer players. Table 2.1 shows the number of participants for each year of the duration of the study and the age range.

The data acquisition protocol adopted in this study follows the methodology described by Minetto et al. [13]. This study visit was conducted as part of the preseason investigations and included measurements of body weight and height, whole-body DXA scan, and acquisition of 3DO whole-body scans. Body weight and height were measured while the subject was wearing underwear and with bare feet. Body weight and height were measured using a standard scale with stadiometer (model Seca 799, Seca GmbH & Co. Kg, Hamburg, Germany). A whole-body DXA scan was performed on a Lunar iDXA system (GE Healthcare, Chicago, IL, USA) according to a standardized protocol. Only one DXA scan was acquired to be radiation dose conserving.

Table 2.1: Number of participants and median age (1st-3rd quartile) by year and sex.

Year	Male participants	Male age	Female participants	Female age
2022	122	16.3 (15.0-18.4) years	68	15.5 (14.5-17.1) years
2023	131	16.2 (14.9-18.0) years	45	16.0 (15.3-16.8) years
2024	17	20.9 (19.9-22.7) years	46	16.2 (15.4-16.9) years

The 3DO scans were acquired via Mobile Fit app (Size Strem LLC, Cary, NC, USA) using a standardized positioning protocol. Each player was guided into position for the self-scan using voice commands from the app. The player was asked to assume a *front A-pose* to capture the frontal image. Next, to capture the lateral image, the player was asked to assume a *side pose*. Subsequent to the image capture, the software produced a de-identified three-dimensional humanoid avatar (Figure 2.1), accompanied by associated anthropometric measurements and body composition estimates. The frontal and lateral images were acquired twice, in order to obtain two avatars for each player. If the experimenters noticed movements of the trunk or limbs during the frontal image capture or improper placement of the upper limbs and hands during the lateral image acquisition, the acquisition was repeated. Body movements or improper placement of the upper limbs might produce changes in the shape of the avatar that can result in biased estimation of various body circumferences.

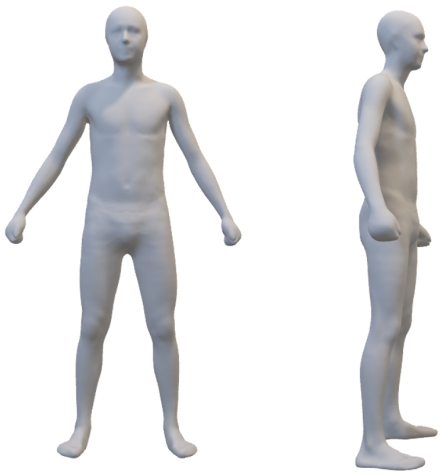

Figure 2.1: Example of a three-dimensional humanoid avatar generated by the Mobile Fit app software.

2.2 Data Sources and Instruments

The following section provides a detailed description of the data sources and instruments used in this study. It includes an overview of the 3DO whole-body scans acquired via Mobile Fit app, the anthropometric measurements and body composition estimates automatically extracted from the Size Stream platform, and the DXA variables that were chosen as ground truth for prediction. These tools

and datasets form the foundation for the subsequent processing steps and the development of predictive models using regression-based machine learning methods.

2.2.1 Three-Dimensional Optical Whole-Body Scans

As reported in the previous section, the 3DO whole-body scans were acquired via Mobile Fit app. Starting from two images, the software produced a three-dimensional humanoid avatar. This avatar can be downloaded in OBJ format. From 2022 to 2024, 853 3DO whole-body scans (avatars) were acquired. There are nine cases where only one 3DO whole-body scan per subject is available, and three where there are more than two 3DO whole-body scans available per subject.

Two different analyses were carried out on the avatars: raw A-pose and T-pose. In the first case, the 3DO scans were used as they are provided by Size Stream. No pre-processing has been applied. The male mesh topology comprised 49,758 vertices and 99,512 faces, while the female mesh included 49,402 vertices and 98,800 faces. For this reason, it was possible to work directly with raw data, without any need for standardization (Figure 2.2).

For the T-pose analysis, the raw 3DO whole-body scans were sent to Meshcapade (Meshcapade GmbH, Tübingen, Germany) to be reposed. The Meshcapade algorithm processes raw 3DO whole-body scans of any size and vertex order, and converts them into meshes containing 10,475 vertices and 20,908 faces. This means that the meshes are now standardized and it is potentially possible to use 3DO scans acquired with different instrumentation. The meshes are reposed so that each individual assumes a standardized T-pose, where the arms are extended horizontally in line with the torso, and both arms and legs are fully straightened (Figure 2.3). Stylized representations are used to substitute areas such as the hands, feet and face. A comprehensive explanation of the Meshcapade processing pipeline is provided by Loper et al. [46]. Generally speaking, for each subject, except those mentioned above, there was a pair of raw 3DO scans in A-pose and a pair of 3DO scans in T-pose, processed by Meshcapade.

2.2.2 Anthropometric Measurements

Size Stream provides four CSV files, along with the subject's avatar. These files contain anthropometric measurements, including circumferences, lengths, volumes, surface areas, and body composition estimates.

The following parameters are reported in the `App Measures.csv` file: BMI, total bone mineral content, body fat (BF) percentage, fitness index, lean body mass, arms lean mass, legs lean mass, shoulder width, visceral adipose tissue, waist-to-hip-ratio, weight, circumferences of neck, chest, underbust, overarm, biceps, forearms, wrists, stomach, seat, thighs, calves, waist, pant waist, hips, back-neck-to-waist length,

sleeves length, crotch length, inseam, outseams, and body surface area.

The `Body Composition.csv` file reports the following parameters: BF percentage, BMI, body surface area, bone mineral content (BMC), fat mass index, fitness index, height, lean body index, lean body mass, arms lean mass, legs lean mass, resting metabolic rate, stomach circumference, visceral adipose tissue, waist circumference, waist-to-height-ratio, waist-to-hip-ratio, weight.

There are two `Core Measures.csv` files, one that reports measurements according to the metric system and the other that reports measurements according to the imperial system. The anthropometric measurements reported in these files can be found in the manual provided by Size Stream, along with their definitions [47].

The body composition estimates are obtained by using proprietary algorithms, with the exceptions of the basal metabolic rate and the BF (%) estimation [2]. These estimates are obtained, respectively, according to the Katch-McArdle equation [48] and to the two equations previously developed and validated by Harty et al. [49].

2.2.3 DXA Variables

The DXA outputs were documented and stored in databases constructed using Microsoft Excel. Among all available parameters, the following six body composition variables were selected for prediction:

1. **Body fat (BF) percentage**: (Total fat mass/Estimated weight) × 100;
2. **Total lean mass (kg)**: Total lean soft tissue + Total BMC;
3. **Appendicular lean soft mass (kg)**: Lean soft mass of the right arm + left arm + right leg + left leg;
4. **Lean soft mass arms (kg)**: Lean soft mass of the right arm + left arm;

Figure 2.2: Standard A-pose on Mobile Fit app.

Figure 2.3: Reposed meshes in a standardized T-pose.

5. **Lean soft mass legs (kg)**: Lean soft mass of the right leg + left leg;
6. **Total fat mass (kg)**.

Within the context of a body composition analysis on a population of young soccer players, these measurements can be particularly useful for optimizing nutritional programs and for identifying potential underlying medical conditions, such as eating disorders [13]. Given their clinical relevance, these variables were chosen as ground truth for training and evaluating the multiple linear regression models developed in this study.

2.3 Data Processing and Analysis

This section provides an in-depth overview of the data processing methods and analytical procedures adopted in this study. All analysis were performed using `MATLAB` (MathWorks, Natick, MA, USA). Figure 2.4 illustrates a schematic representation of the developed pipeline, highlighting each step from the import of raw data to the development of the models. This methodology was first performed for the avatars in A-pose, and then for the avatars in T-pose. The following sections describes the methodology considering only one case study. However, the results of the intermediate steps for both cases are reported.

A brief explanation of each step is provided below:

- **Import of 3DO whole-body scans**: import of each avatar, in A-pose and T-pose, into `MATLAB`.
- **Import of anthropometric and DXA variables**: import of Anthropometric and DXA variables into `MATLAB`, from CSV and XLSX (Excel) files.

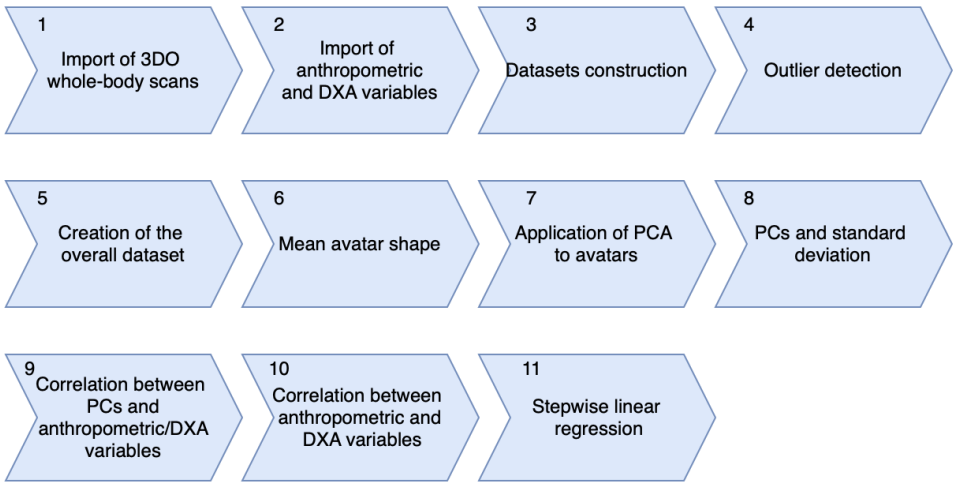

Figure 2.4: Schematic representation of the data processing and analysis pipeline of this study.

- **Datasets construction**: duplicate avatars and anthropometric variables of each subject are averaged in order to have one observation per subject, and they are associated with their respective DXA file.
- **Outlier detection**: application of outlier detection to the values of anthropometric and DXA variables.
- **Creation of the overall dataset**: the datasets of the three years are merged so that the overall dataset is obtained.
- **Mean avatar shape**: calculation of the mean male and female avatar shape.
- **Application of PCA to avatars**: application of PCA to the vertices of the meshes.
- **PCs and standard deviation**: the morphological variations associated with each PCs are highlighted, starting from the mean avatar shape.
- **Correlation between PCs and anthropometric/DXA variables**: calculation of the correlation matrix between PCs and anthropometric/DXA variables.
- **Correlation between anthropometric and DXA variables**: calculation of the correlation matrix between anthropometric and DXA variables.

- **Stepwise linear regression**: construction of multiple linear regression models for the prediction of the chosen DXA variables, as reported in Section 2.2.3.

2.3.1 Pre-Processing and Dataset Construction

The 853 3DO whole-body scans and associated files, containing anthropometric measurements, body composition estimates, and DXA variables, were divided according to the year of acquisition. The rationale for executing the pre-processing steps independently on separate years is as follows: given the protracted nature of this analysis over the years, it happened that the same subjects showed up in multiple years during the course of the acquisition campaign. Consequently, it was determined that these individuals should be considered as separate subjects. This is due to the fact that, following a year of growth, substantial differences in terms of shape are observed among young athletes. Working separately between years avoids confusion and grouping together 3DO whole-body scans and files that should not be. Once this initial separation was made, another division for males and females was carried out. Table 2.2 shows the number of 3DO whole-body scans by year and sex. The final regression models will be different between the two sexes, even if the target is the same.

Each OBJ was loaded into `MATLAB`. The vertices, whose coordinates were used to perform PCA, have been saved. At the end of this process, a matrix of size $(3 \times N) \times$ num_scans was obtained, where N identifies the number of vertices and num_scans the number of 3DO scans.

As previously mentioned, the Size Stream platform provides four CSV files along with each scan. For this study, the `Core Measures Metric.csv` and the `Body Composition.csv` were imported into `MATLAB`.

From the `Core Measures Metric.csv` file, the following anthropometric variables were selected:

- **Circumferences** (cm): waist, hip, arm, thigh, chest, wrist, neck, abdomen, knee, calf, head, forearm, collar, upper arm, ankle, right thigh.
- **Surface areas** (cm^2): arm, leg.

Table 2.2: Number of 3DO whole-body scans by year and sex.

Year	Male 3DO scans	Female 3DO scans
2022	242	136
2023	262	90
2024	30	93

- **Volumes** (cm^3): arm, torso, leg.
- **Outside leg length** (cm).
- **Muscle-to-stomach index (MSI)**:

$$\frac{(\text{right + left bicep circ.}) + (\text{right + left calf circ.}) + (\text{right + left thigh circ.})}{\text{stomach max circ.}}$$

The circumferences and lengths of the left and right sides of the body were averaged to obtain a single value. The volumes and surface areas of the left and right sides of the body were summed. These anthropometric variables were chosen because they are related to lean and fat mass estimation, as demonstrated by the equations proposed by Harty and McCarthy, shown in Table 2.3.

Table 2.3: Equations for estimating BF (%) and appendicular lean mass (ALM) proposed by Harty and McCarthy. Units of measurements: cm (circumferences and lengths), cm^2 (areas), cm^3 (volumes), kg (weight), and years (age). NHOPI: Native Hawaiian and Other Pacific Islander. Adapted from Minetto et al. [13].

Variable	**Equation**	**Refs**
BF (%)	$48.837 - 7.2745 \times (1 \text{ for male, } 0 \text{ for female}) + 0.46929 \times (\text{right thigh circ.}) - 17.387 \times (\text{muscle-to-stomach index})$	[49]
ALM (kg) — male	$-27.386 + 2.566 \times (1 \text{ for NHOPI race}) + 0.132 \times \text{height} + 0.221 \times \text{weight} + 0.068 \times (\text{head circ.}) + 0.087 \times (\text{chest circ.}) + 0.212 \times (\text{forearm circ.}) - 0.038 \times (\text{waist circ.}) + 0.020 \times (\text{thigh circ.}) - 0.024 \times (\text{outside leg length}) + 0.0008 \times (\text{surface area arm}) + 0.00005 \times (\text{arm volume}) - 0.0002 \times (\text{torso volume}) + 0.0003 \times (\text{leg volume})$	[50]
ALM (kg) — female	$-12.622 - 0.023 \times \text{age} - 0.191 \times (1 \text{ for Caucasian}) + 0.427 \times (1 \text{ for Black}) - 0.288 \times (1 \text{ for Hispanic}) + 0.553 \times (1 \text{ for NHOPI}) - 0.709 \times (1 \text{ for Other race}) + 0.088 \times \text{height} + 0.135 \times \text{weight} + 0.001 \times (\text{head circ.}) + 0.019 \times (\text{collar circ.}) + 0.048 \times (\text{forearm circ.}) + 0.078 \times (\text{upper arm circ.}) - 0.039 \times (\text{waist circ.}) + 0.083 \times (\text{ankle circ.}) + 0.023 \times (\text{outside leg length}) + 0.0003 \times (\text{surface area leg})$	[50]

From the `Body Composition.csv` file, the following body composition estimates were selected:

- **Height** (cm);
- **Weight** (kg);
- **Fitness Index**.

According to Size Stream [51], the Fitness Index offers a comprehensive metric for tracking health and fitness. By combining muscle mass, body measurements, and BF (%), it offers a more complete picture than metrics like BMI. The index includes torso and limbs measurements, including waist circumference to account for visceral and subcutaneous fat. It captures essential data on muscle and fat.

The Excel files containing the DXA outputs were imported into `MATLAB`. Then, the variables discussed in Section 2.2.3, which will constitute the targets of the regression models, were extracted and calculated.

At the end of this process, 26 anthropometric variables and body composition estimates were selected, 6 target variables were chosen, and the matrices of vertices were obtained.

As mentioned above, two 3DO scans per subject were available in almost all cases. This means that for each scan, there were the corresponding CSV files, while the DXA scan was performed only once.

At this point, it was necessary to create a dataset with a single observation per subject. For each individual, the 3DO whole-body scans were averaged, as well as the anthropometric variables extracted from the corresponding CSV files. As a result, each subject was represented by a unique avatar, a single row of anthropometric measurements, and the corresponding DXA variables.

The final pre-processing step consisted of outlier detection. After verifying the normality of the data using the Kolmogor-Smirnov test, the Grubbs's test was applied to identify outliers in the anthropometric and DXA variables. Subjects identified as outliers were removed from the dataset to ensure consistency for the analysis to follow.

Grubbs's test (published by Frank E. Grubbs [52]) is a statistical method designed to identify a single outlier in a sample that is assumed to follow a normal distribution. The objective is to determine whether the dataset contains at least one value that deviates substantially from the mean and can therefore be considered an outlier. The hypotheses tested are as follows:

- **Null hypothesis** (H_0): no outliers are presented in the dataset.
- **Alternative hypothesis** (H_1): there is exactly one outlier in the dataset.

The test computes a statistic G defined as:

$$G = \frac{\max\limits_{i=1,\dots,N} \left| Y_i - \overline{Y} \right|}{s} \tag{2.1}$$

with $\overline{Y}$ and s denoting, respectively, the sample mean and standard deviation. G measures how far the most extreme value in the dataset is from the sample mean, normalized by the standard deviation. This value is then compared to a critical threshold derived from the Student's t-distribution, at a given significance level (5% in this study)

$$G > \frac{N-1}{\sqrt{N}} \sqrt{\frac{t^2_{\alpha/(2N),N-2}}{N-2+t^2_{\alpha/(2N),N-2}}} \tag{2.2}$$

where $t^2_{\alpha}/(2N), N-2$ represents the upper critical value from the t-distribution with $N-2$ degrees of freedom, corresponding to a significance level of $\alpha/(2N)$. If G exceeds the critical value, the corresponding observation is considered an outlier. An iterative approach was performed, since this method detects one outlier at a time for each column (variable).

Table 2.4 shows the number of observations left after the outlier detection performed with the Grubbs's test. In 2022 three male athletes and one female athlete were removed; in 2023 three male athletes and one female athlete were removed; in 2024 two male athletes and one female athlete were removed.

Since the pre-processing steps were carried out separately for the three years, it was necessary to merge the three datasets to obtain the overall dataset. This final dataset consisted of 262 male observations and 156 female observations. This was valid for both avatars in A-pose and avatars in T-pose.

2.3.2 Principal Component Analysis (PCA)

Subsequent to the processing and organization of all data, the next step was to perform a PCA. Prior to this, the mean avatar shape was computed for both male and female participants. This process involved calculating the mean of each vertex coordinate across all subjects. More specifically, for every corresponding vertex in the mesh, the average position in three-dimensional space (x,y,z) was computed over the entire dataset. The resulting vector of averaged coordinates represented the vertices of the mean avatar shape. From this vector, a three-dimensional mesh was reconstructed. However, while computing the average shape of the avatars in

Table 2.4: Number of observations remaining after outlier detection by year and sex.

Year	Male observation	Female observation
2022	119	67
2023	128	44
2024	15	45

A-pose, a critical issue arose. The vertex order in the 2024 OBJ files provided by Size Stream differs from that of the 2022 and 2023 files. As a result, the mean shape reconstruction appeared corrupted, as shown in Figure 2.5. Therefore, it was decided to exclude all 2024 A-pose OBJ, CSV and, DXA files from the subsequent steps, to prevent further complications in the analysis. This issue did not occur with the T-pose avatars standardized by Meshcapade, as they share an equal number and ordering of vertices. From this point onward, the datasets of the avatars in A-pose will differ from the datasets of the avatars in T-pose.

Figure 2.6 and Figure 2.7 provide a representation of the average shape within each population.

Given the high correlation between neighboring vertices in a three-dimensional body mesh, PCA was applied to perform dimensionality reduction and to transform the mesh data into an orthogonal basis [30]. The algorithm was independently applied to male and female datasets of the avatars, and it was also extended to anthropometric measurements in a successive analysis. A detailed explanation of the mathematical formulation of PCA is provided in Appendix A, while the procedures specific to anthropometric variables are described in Appendix B.

`MATLAB` performs the PCA following the singluar value decomposition (SVD) approach by default and returns the loadings matrix, the scores matrix and the percentage of total variance explained by each PC. As shown in Figure 2.8, seven PCs described 95% of the shape variance (a commonly adopted threshold in

Figure 2.5: Corrupted male average shape (on the left) and female average shape (on the right) of the avatars in A-pose (2022-2023-2024).

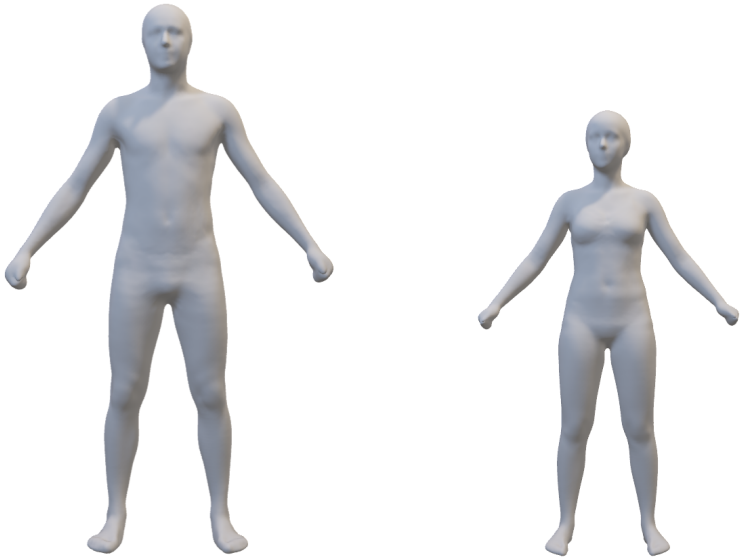

Figure 2.6: Male average shape (on the left) and female average shape (on the right) of the avatars in A-pose (2022-2023).

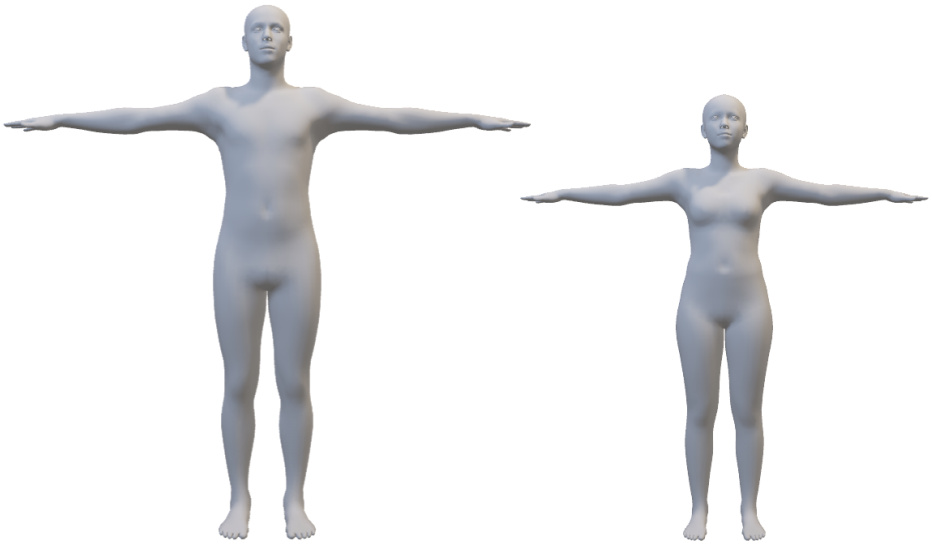

Figure 2.7: Male average shape (on the left) and female average shape (on the right) of the avatars in T-pose (2022-2023-2024).

dimensionality reduction) in the male A-pose dataset and six PCs described 95% of the shape variance in the female A-pose dataset. Figure 2.9 shows that the first PC described 95% of the shape variance in both male and female T-pose datasets.

From the average body shape of each population, morphological deformations were applied along the principal directions identified by the PCA. These deformations were generated by adding and subtracting three standard deviations to each PC, thereby highlighting the morphological variation represented by each component. This approach offers an intuitive visualization of the dominant shape patterns in the datasets.

A total of seven PCs were selected for visualization, both for male and female subjects and for avatars in A-pose (Figure 2.10 and Figure 2.11) and T-pose (Figure 2.12 and Figure 2.13). This number was chosen because seven was the highest number of PCs needed to explain at least 95% of the total body shape variance across all datasets. For consistency, the same number of PCs was applied to each dataset.

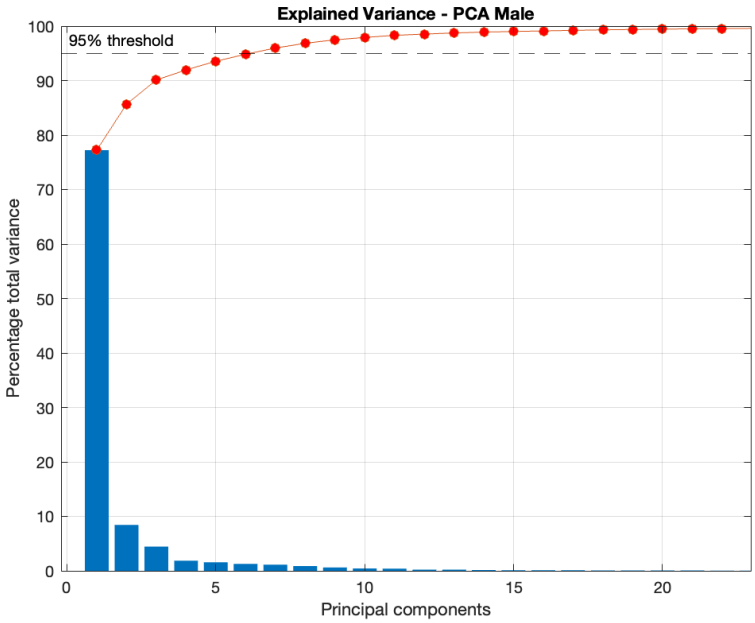

(a) Explained variance – Male

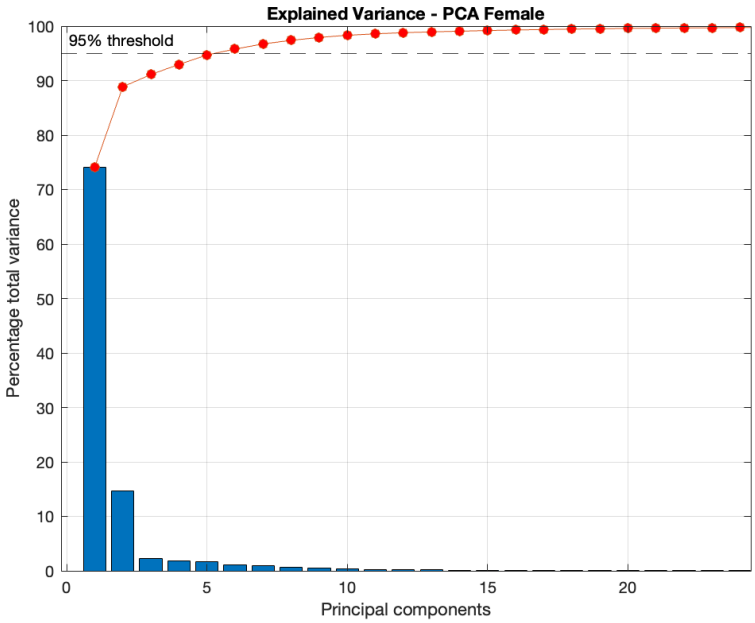

(b) Explained variance – Female

Figure 2.8: Percentage of total variance explained by each PC for male (a) and female (b) avatars in A-pose.

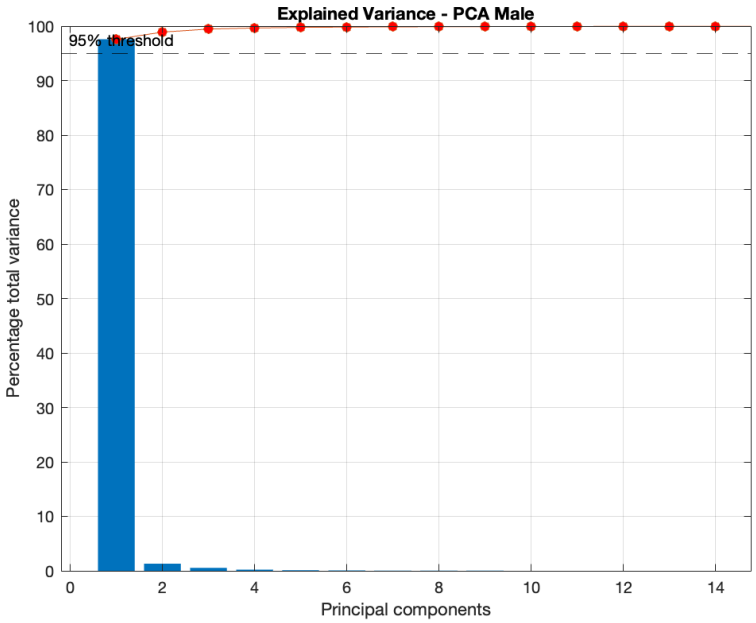

(a) Explained variance – Male

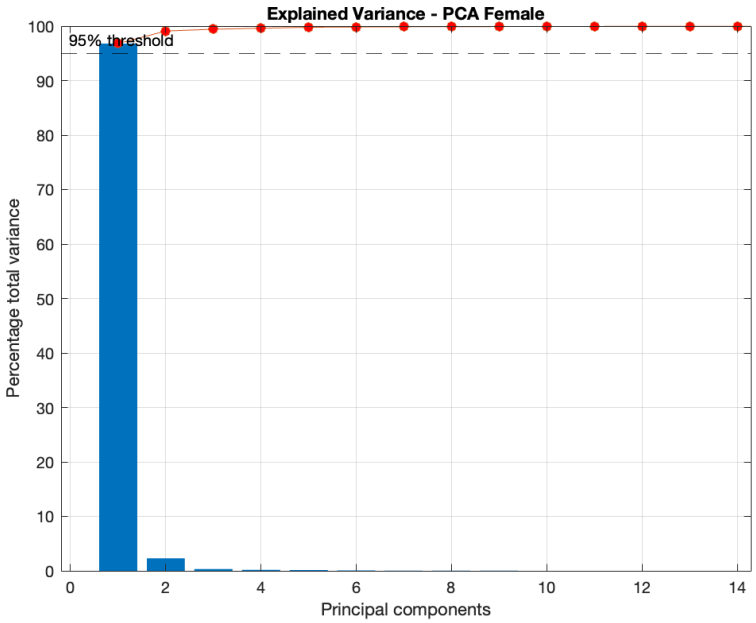

(b) Explained variance – Female

Figure 2.9: Percentage of total variance explained by each PC for male (a) and female (b) avatars in T-pose.

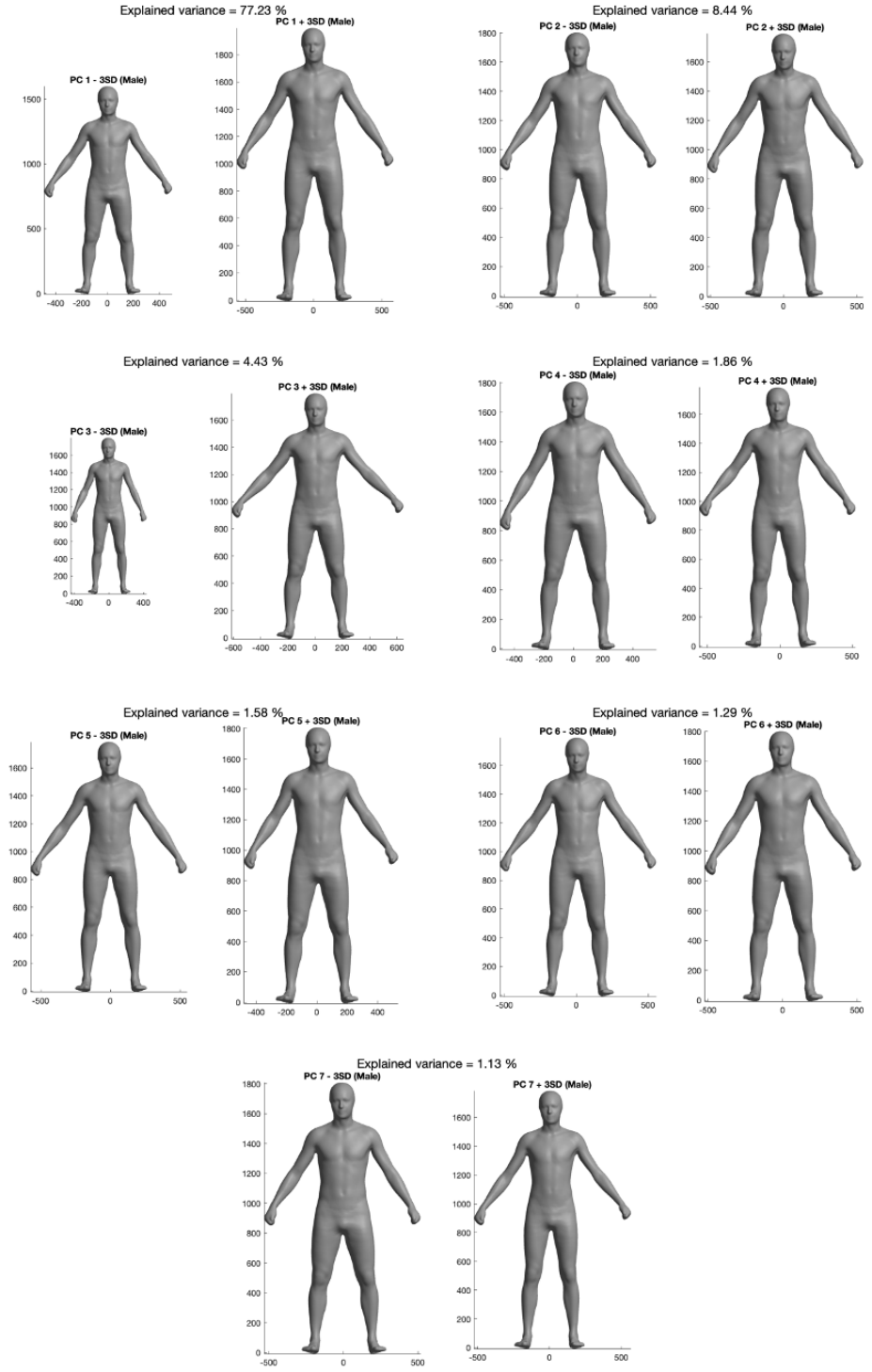

Figure 2.10: Morphological variation represented by the first seven PCs for the male avatars in A-pose.

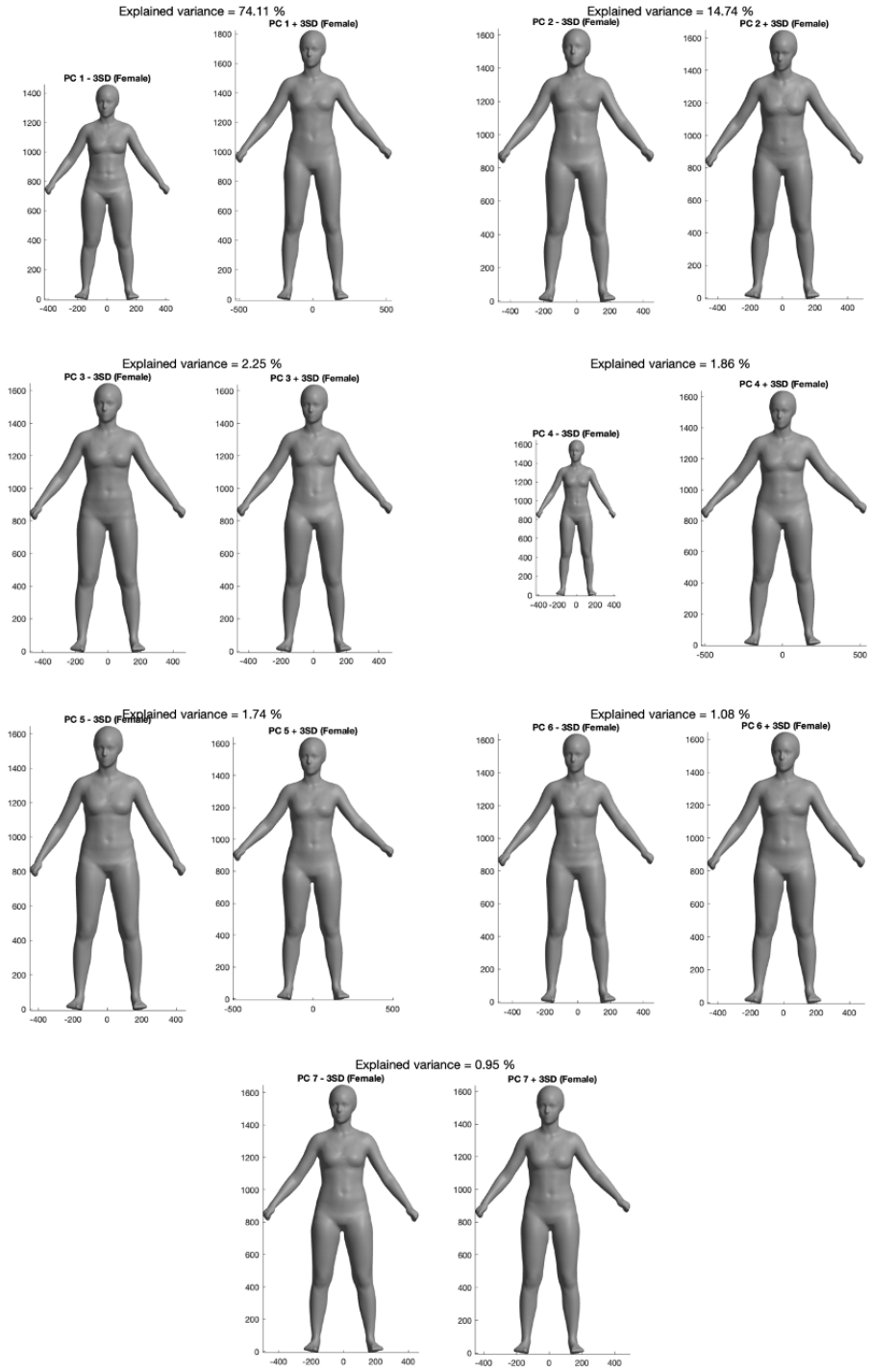

Figure 2.11: Morphological variation represented by the first seven PCs for the female avatars in A-pose.

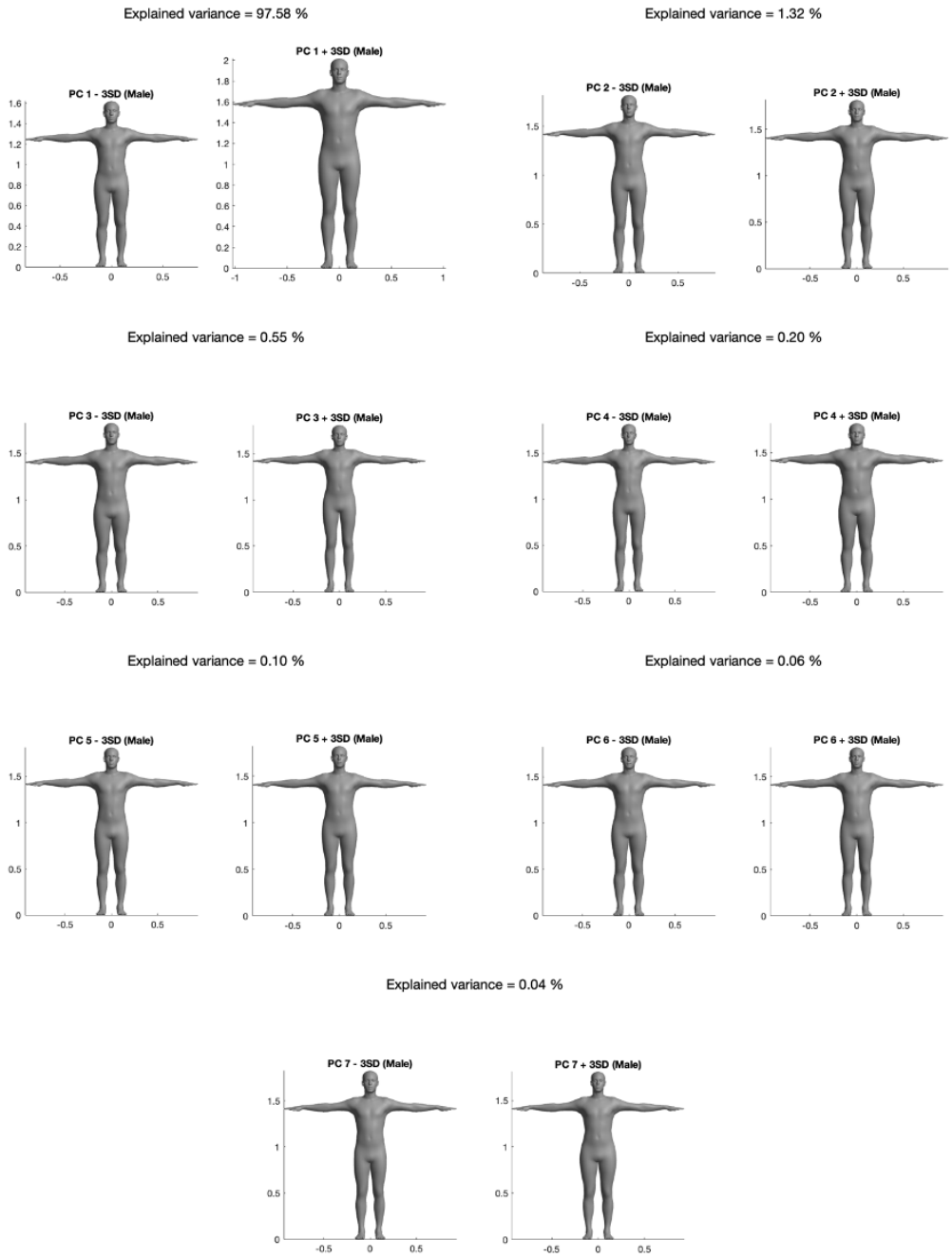

Figure 2.12: Morphological variation represented by the first seven PCs for the male avatars in T-pose.

Figure 2.13: Morphological variation represented by the first seven PCs for the female avatars in T-pose.

To evaluate the relationship between the morphological features identified by the PCs and the anthropometric/DXA variables, Pearson's correlation coefficients were calculated. Specifically, the first seven PCs were correlated with all anthropometric and DXA variables. The resulting correlation matrix was visualized as a heatmap. Only statistically significant correlations, with P values < 0.05, were maintained, while non significant coefficients were replaced with Not a Number (NaN). Each cell in the heatmap represents the correlation coefficient between a given PC and a specific variable, enabling immediate identification of the most influential components and their associated measurements.

Figure 2.14 shows that PC1 was significantly correlated with nearly all anthropometric and DXA variables in both male and female shape models of the A-pose avatars. In the female dataset, additional significant correlations were observed for PC4 and PC6.

Similarly, Figure 2.15 illustrates that PC1 also displayed strong and consistent correlations across all variables for the T-pose avatars. In the male dataset, PC2 and PC4 demonstrated notable associations, although weaker.

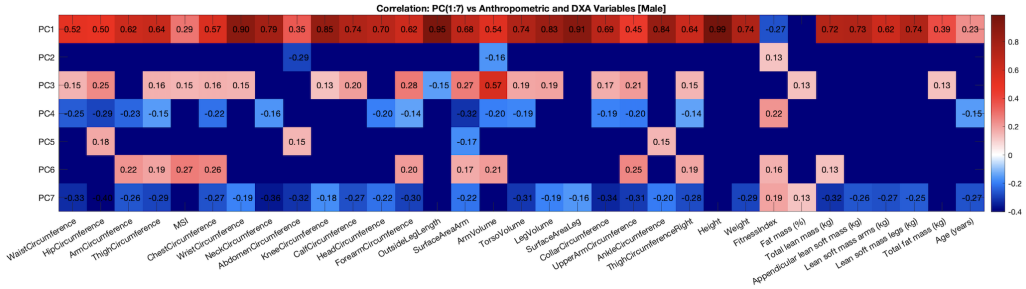

(a) Correlation matrix - Male

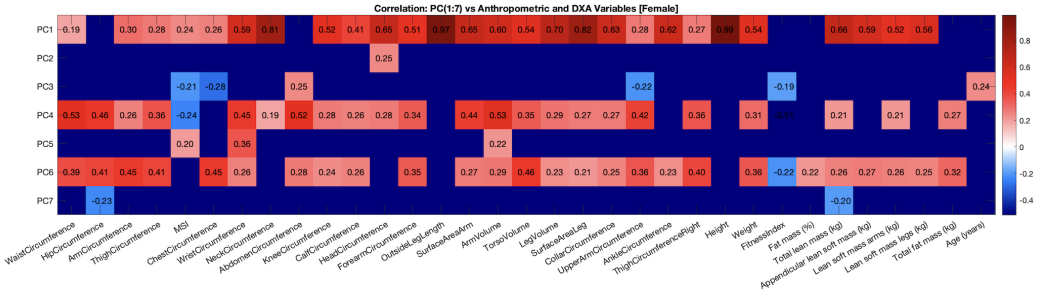

(b) Correlation matrix - Female

Figure 2.14: Correlation matrix between PCs and anthropometric/DXA variables for male (a) and female (b) avatars in A-pose.

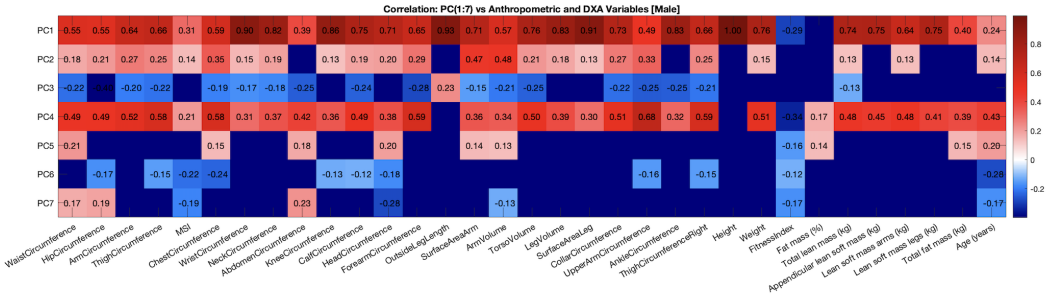

(a) Correlation matrix - Male

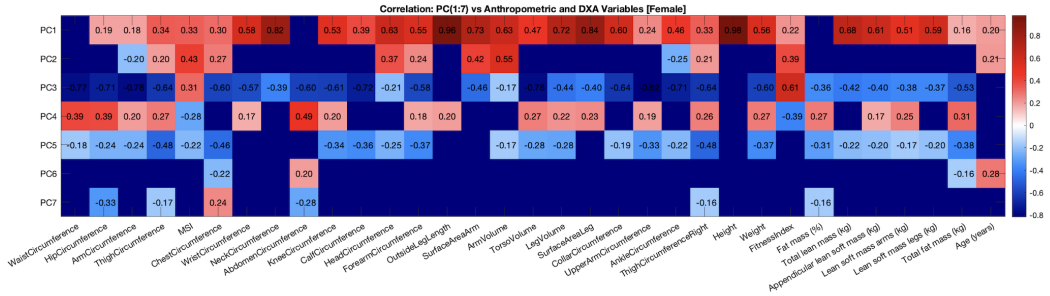

(b) Correlation matrix - Female

Figure 2.15: Correlation matrix between PCs and anthropometric/DXA variables for male (a) and female (b) avatars in T-pose.

Additionally, a scatter plot was generated for each sex to illustrate the relationship between PC1 and the variable with the highest absolute correlation with it. A least squares regression line was added to show the strength and direction of the association. As shown in Figure 2.16 and Figure 2.17, height was always the most highly correlated variable with PC1.

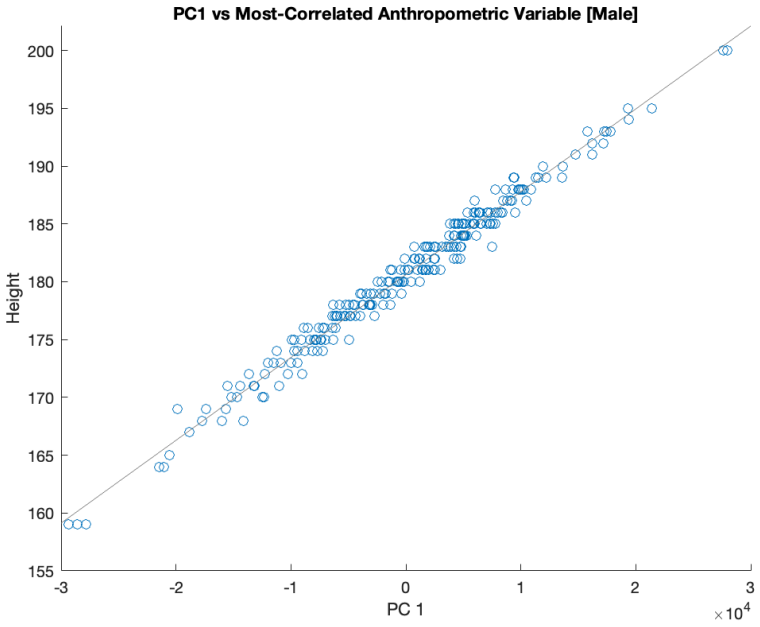

(a) Scatter plot - Male

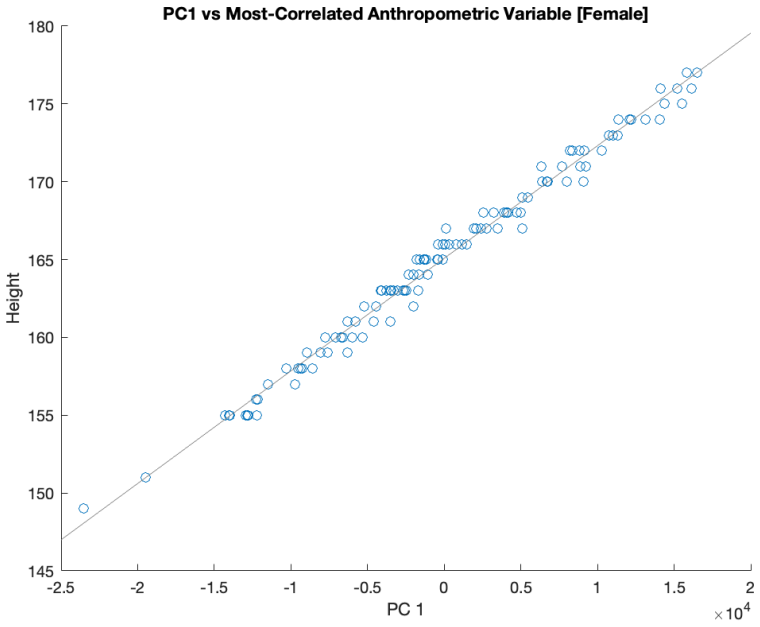

(b) Scatter plot - Female

Figure 2.16: PC1 vs most-correlated anthropometric variable for male (a) and female (b) avatars in A-pose.

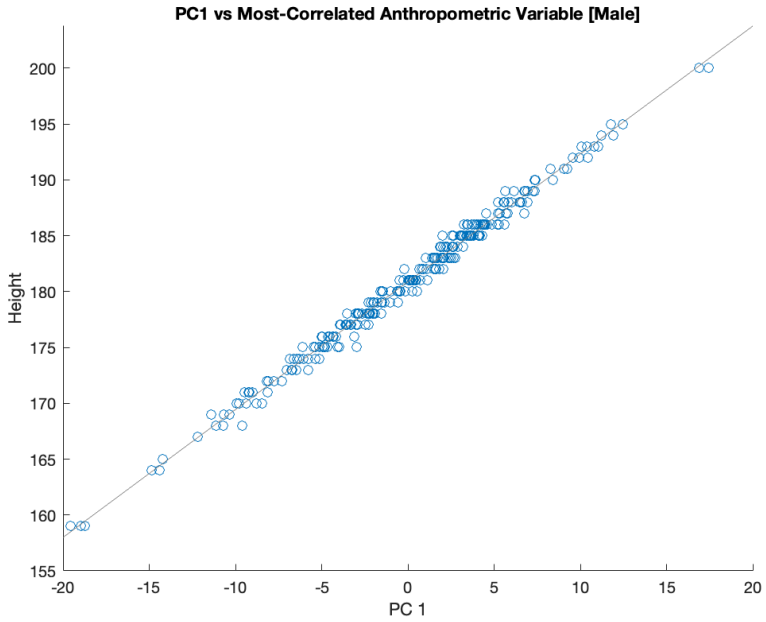

(a) Scatter plot - Male

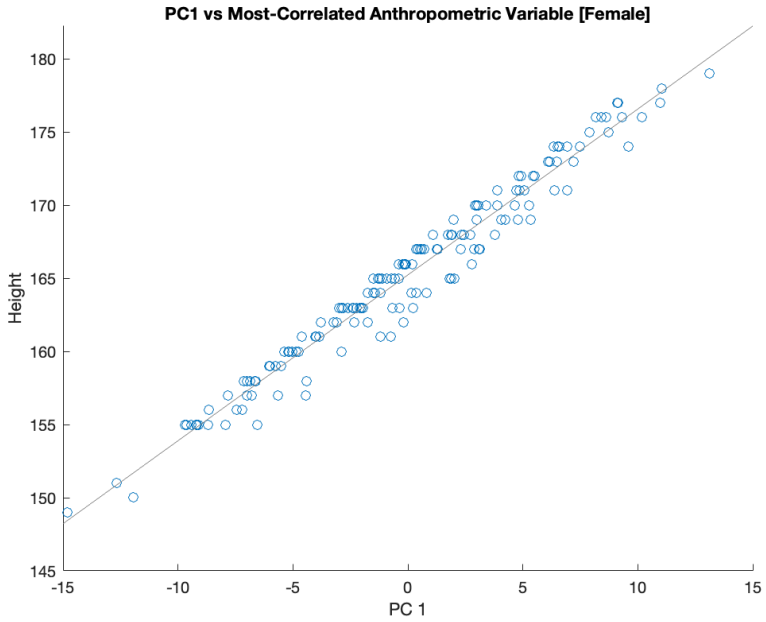

(b) Scatter plot - Female

Figure 2.17: PC1 vs most-correlated anthropometric variable for male (a) and female (b) avatars in T-pose.

To further explore the associations between anthropometric measurements and body composition, Pearson's correlation coefficients were also computed between the anthropometric and DXA variables. Only statistically significant correlations were maintained (P value < 0.05), while non significant values were replaced with NaN.

Although this analysis was performed for both the A-pose and T-pose avatars, the resulting correlation matrices were not identical. As previously explained, the A-pose dataset only included subjects from 2022 and 2023 due to inconsistencies in the 2024 OBJ files, which explains this discrepancy. In contrast, the T-pose dataset included subjects from all three years. As shown in Figure 2.18 and Figure 2.19, BF (%) shows little to no correlation with most anthropometric measurements in male datasets. This suggest that fat distribution may not be easily captured.

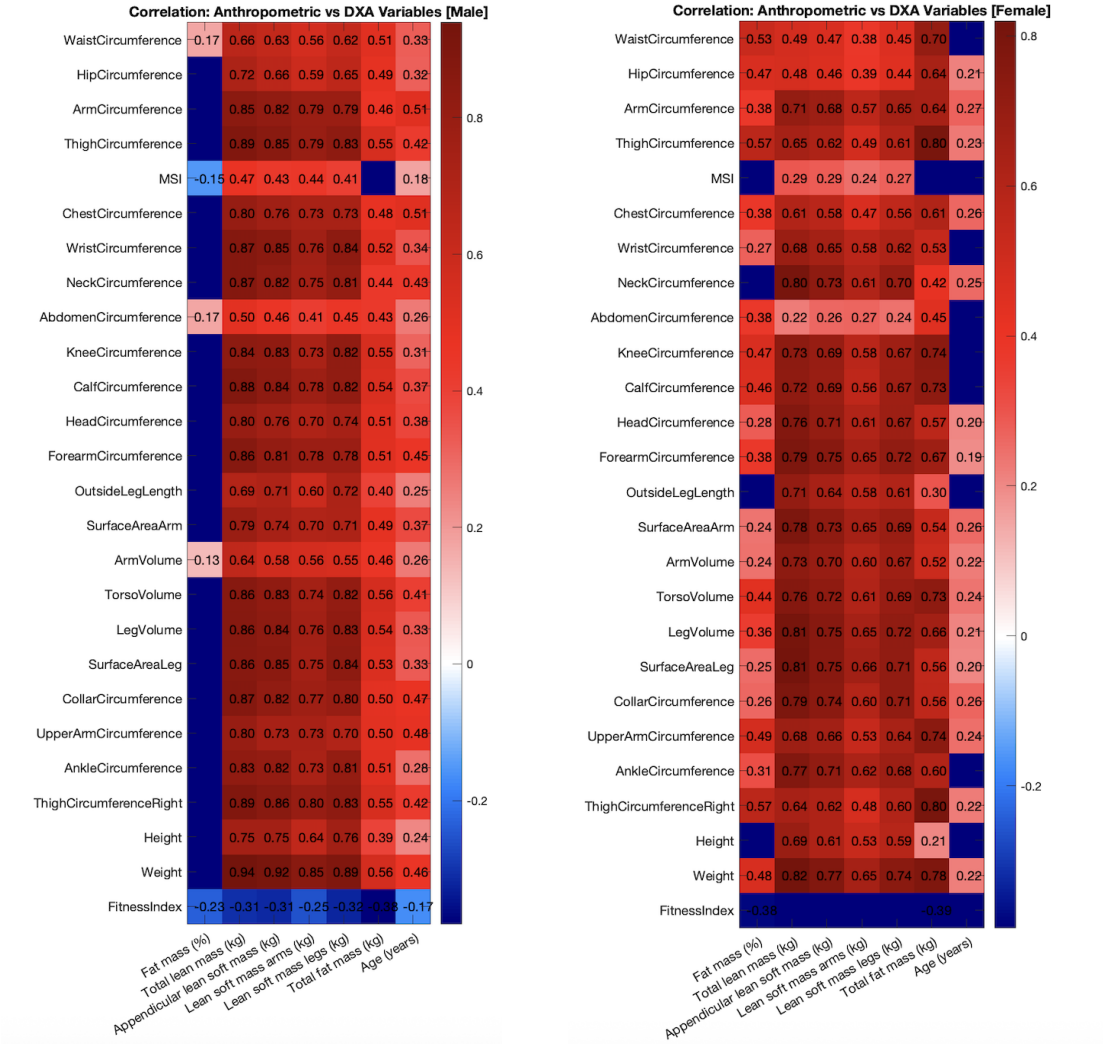

(a) Correlation matrix - Male **(b)** Correlation matrix - Female

Figure 2.18: Correlation matrix between anthropometric and DXA variables for male (a) and female (b) avatars in A-pose.

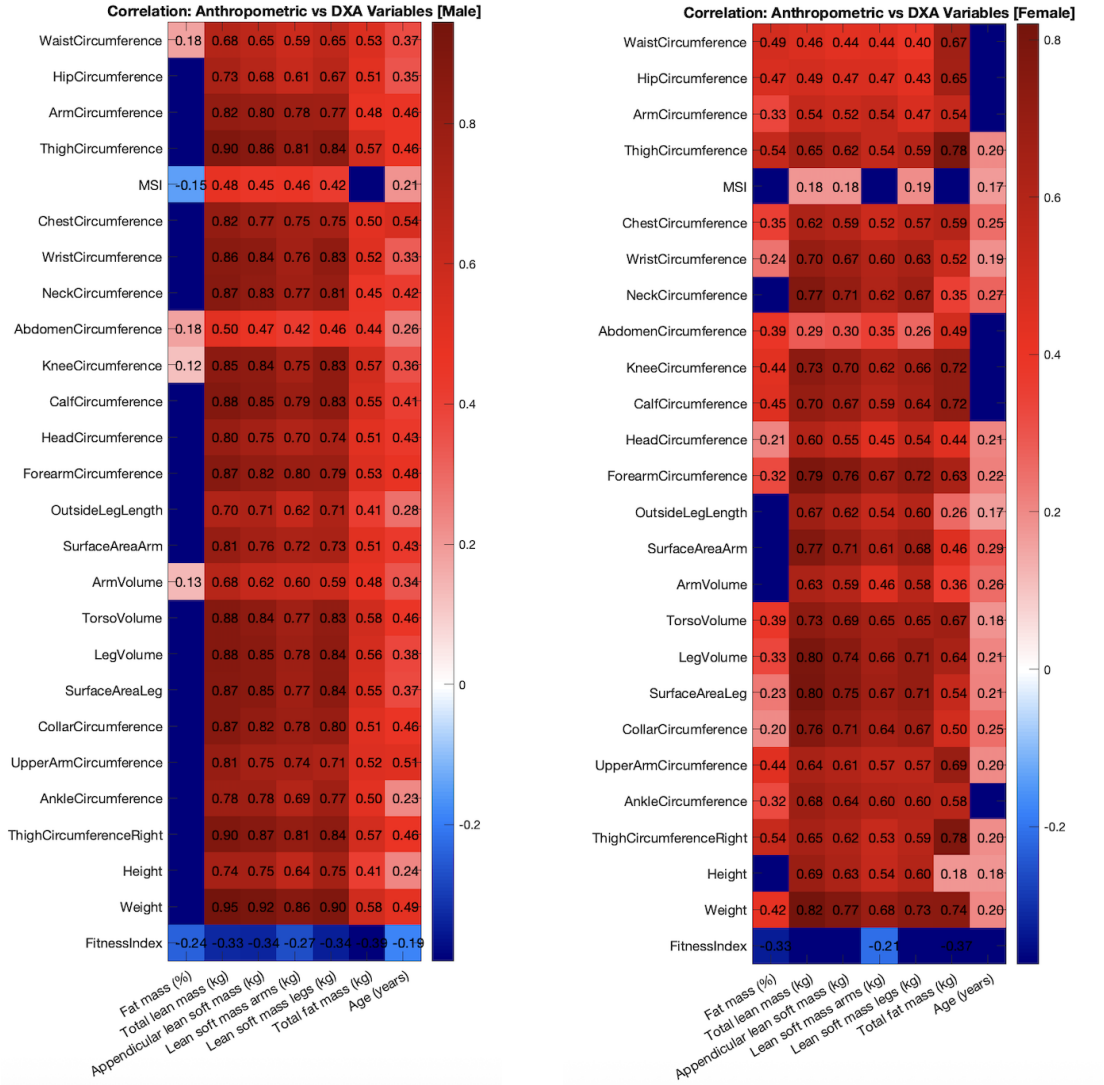

(a) Correlation matrix - Male **(b)** Correlation matrix - Female

Figure 2.19: Correlation matrix between anthropometric and DXA variables for male (a) and female (b) avatars in T-pose.

2.3.3 Stepwise Linear Regression

Following the application of PCA and related analysis, multiple linear regression models were developed to predict six DXA variables (dependent variables): body fat (BF) percentage, total lean mass (kg), appendicular lean soft mass (kg), lean soft mass arms (kg), lean soft mass legs (kg), total fat mass (kg). The independent variables were the PCs and the anthropometric measurements.

The datasets, which include PCA scores, anthropometric variables, and DXA targets, were randomly divided into training (80%) and test (20%) sets, making sure that the observations of the same subjects were entirely on either the training or the test set. To ensure the reproducibility and comparability of the models, a fixed seed was set. This kept the partitions of the training and test sets identical across all experiments.

The performance of the models was evaluated using fivefold cross-validation applied to the training set. In fivefold cross-validation, the training set is divided into five parts of similar size (fold). In each iteration, four folds are used for training and one fold is used for internal testing. The procedure is repeated five times, changing the test fold each cycle. This ensure that all training data is used once as an internal test and four times for training. This approach reduces the risk of overfitting by evaluating how well the model generalizes to unseen data within the training set.

The number of PCs tested varied from 3 to 20 to determine the optimal compromise between performance and model complexity.

Variable selection was performed using a stepwise regression approach that combined forward and backward selection to minimize the Bayesian Information Criterion (BIC).

The BIC is a criterion used to choose the best model from a set of possible models. Models with lower BIC values are usually preferred. While it is possible to increase the maximum likelihood by adding parameters when fitting models, doing so may result in overfitting. BIC attempts to address this problem by introducing a penalty term for the number of parameters in the model. It was developed by Gideon Schwarz [53] and it is defined, for a model estimated on a dataset of n observations and k parameters, as:

$$BIC = k \ln(n) - 2 \ln(\widehat{L}) \tag{2.3}$$

with $\widehat{L}$ denoting the maximum likelihood value of the model.

The term $k \ln(n)$ penalizes the complexity of the model (number of parameters) as the dataset size increases.

The term $-2 \ln(\widehat{L})$ assesses how well the model fits the data.

A lower BIC indicates a reasonably accurate fit, but with not too many parameters.

Considering both A-pose and T-pose avatars, a total of six models were created for each DXA outcome and for each sex using:

- only PCA scores of the avatars (A-pose and T-pose);
- only anthropometric variables;
- a combination of PCA scores of the avatars (A-pose and T-pose) and anthropometric variables;
- only PCA scores of the anthropometric measurements (Appendix B).

2.4 Statistical Methods

The accuracy of each model was measured using the coefficient of determination (R^2) and root mean square error (RMSE).

2.4.1 Coefficient of Determination (R^2)

The coefficient of determination (R^2) is a measure that provides information about how well a model fits the data. In the context of regression, it is a statistical measure of how closely the regression line approximates the actual data [54]. The measure is defined as follows:

$$R^2 = 1 - \frac{\sum_{i=1}^{n}(y_i - \hat{y}_i)^2}{\sum_{i=1}^{n}(y_i - \bar{y})^2} \tag{2.4}$$

where y_i is the observed value, $\hat{y}_i$ is the predicted value, $\bar{y}$ is the mean of the observed values, and n is the number of observations. In this study, the observed values are those of the DXA variable to be predicted (ground truth), and the predicted values are those obtained by applying the model. The numerator represents the sum of squares of residuals, and the denominator represents the total sum of squares. The R^2 ranges from 0 to 1.

Table 2.5 shows the interpretation of the values of the R^2. The best case possible is when the predicted values match exactly the observed values, which results in $R^2 = 1$.

2.4.2 Root Mean Square Error (RMSE)

The root mean square error (RMSE) is defined as the measure of the differences between the values predicted by a model and the values observed [55]. The measure is calculated as follows:

Table 2.5: Interpretation of the values of the coefficient of determination (R^2), adapted from [54].

R^2 values	**Interpretation**
$R^2 = 1$	All the variation in the values of the dependent variable is accounted for by the values of the independent variables
$R^2 = 0.50$	50% of the variation in the values of the dependent variable is accounted for by the values of the independent variables
$R^2 = 0$	None of the variation in the values of the dependent variable is accounted for by the values of the independent variables

$$\text{RMSE} = \sqrt{\frac{1}{n}\sum_{i=1}^{n}(y_i - \hat{y}_i)^2} \tag{2.5}$$

where y_i is the observed value, $\hat{y}_i$ is the predicted value, and n is the number of observations. The predicted and observed values are defined in the same way as in the previous subsection. In general, the smaller the RMSE value generated by a model, the more accurate the model is in predicting the observed values [56].

Chapter 3

Results

This chapter presents the numerical results and prediction equations obtained during the development of the thesis. The metrics presented in Section 2.4 were used to evaluate the accuracy of the results obtained in comparison with DXA e and the applicability of this methodology in a youth sports context to determine whether it can be used as a valid and reliable tool to monitor body composition. Following the outlier detection, a total of 418 observations remained in the analysis. Of these, 262 are male observations and 156 are female. For the A-pose analysis, the 2024 meshes were excluded, leaving a total of 247 male and 111 female observations. The results obtained from the application of fivefold cross-validation on the training set are shown below, followed by those obtained on the test set.

Fivefold cross-validation

After conducting several tests on the training set, it was noted that the maximum number of PCs useful for the construction of the models is 16. Beyond this number, the performance remains unchanged. Figure 3.1 shows an example of plot used to select the optimal number of PCs for the construction of multiple regression models. The mean value of R^2 and RMSE obtained from the application of fivefold cross-validation are plotted in the graph for each PC, in a range from 3 to 20. This representation illustrates the point at which model performance saturates. For this reason, and to ensure comparability between models, 16 PCs will always be used.

Table 3.1 shows the mean results obtained from fivefold cross-validation of 3DO body composition models constructed using A-pose and T-pose meshes. Male body composition models using the T-pose PC-only showed slight improvement over the A-pose PC-only models in terms of R^2 and RMSE in only two cases: total lean mass and total fat mass. In contrast, female body composition models using the T-pose PC-only showed marked improvement across most outcomes. T-pose PC-only models for male body composition reported R^2 values ranging from -0.06,

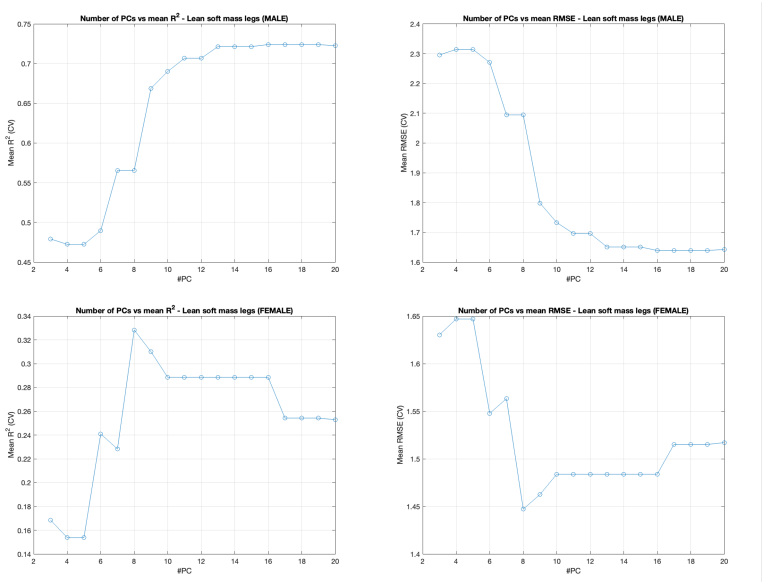

Figure 3.1: Example of plot used to determine the optimal number of PCs for constructing the regression models.

for body fat (BF) percentage, to 0.83, for total lean mass; whereas females reported values ranging from 0.24, for BF percentage, to 0.61, for total lean mass. A-pose PC-only models for males had R^2 values that ranged from 0.03 to 0.82, while females ranged from -0.15 to 0.63. The most significant improvement was the total fat mass estimate in T-pose for males, with an R^2 increasing from 0.24 to 0.27, and an RMSE decreasing from 1.90 kg to 1.87 kg; whereas for the females it was the BF percentage, with an R^2 rising from -0.15 to 0.24 and an RMSE going from 3.82% to 3.32%.

The performance of all but one model (BF percentage) increased substantially when anthropometric variables were included in the models construction. This is valid for both A-pose and T-pose meshes. Male body composition models using the T-pose PC + anthro showed very similar performance to the A-pose PC + anthro models; whereas female body composition models using T-pose PC + anthro showed a moderate improvement. T-pose PC + anthro models for male body composition reported R^2 values ranging from -0.03 (BF percentage) to 0.88 (total lean mass); while females reported values ranging from 0.28 (BF percentage) to 0.68 (total lean mass). The total fat mass estimate worsened using the male T-pose PC + anthro compared to the relative A-pose PC + anthro (R^2 from 0.37 to 0.30, RMSE from 1.73 kg to 1.83 kg). The BF percentage estimate using the female T-pose PC + anthro increased considerably compared to the A-pose PC + anthro (R^2 from 0.09 to 0.28, RMSE from 3.38% to 3.23%).

Table 3.1: 3DO body composition models from stepwise linear regression to predict DXA total and regional body composition. The mean results from fivefold cross-validation are reported for the following models from left to right: PCA scores of the A-pose meshes, PCA scores of the A-pose meshes and anthropometric variables, PCA scores of the T-pose meshes, PCA scores of the T-pose meshes and anthropometric variables.

Outcome	**Sex**	**Model type**			
		A-pose PC-only R^2 / RMSE	A-pose PC + Anthro R^2 / RMSE	T-pose PC-only R^2 / RMSE	T-pose PC + Anthro R^2 / RMSE
BF (%)	M	0.03 / 2.39	-0.02 / 2.45	-0.06 / 2.44	-0.03 / 2.40
	F	-0.15 / 3.82	0.09 / 3.38	0.24 / 3.32	0.28 / 3.23
Total lean mass (kg)	M	0.82 / 3.17	0.86 / 2.72	0.83 / 3.25	0.88 / 2.71
	F	0.63 / 2.20	0.66 / 2.11	0.61 / 2.25	0.68 / 2.03
Appendicular lean soft mass (kg)	M	0.74 / 2.09	0.84 / 1.71	0.74 / 2.27	0.85 / 1.70
	F	0.45 / 1.56	0.55 / 1.42	0.54 / 1.41	0.58 / 1.35
Lean soft mass arms (kg)	M	0.60 / 0.77	0.71 / 0.66	0.60 / 0.80	0.72 / 0.67
	F	0.21 / 0.40	0.23 / 0.40	0.36 / 0.36	0.33 / 0.37
Lean soft mass legs (kg)	M	0.72 / 1.64	0.79 / 1.44	0.67 / 1.92	0.79 / 1.52
	F	0.29 / 1.48	0.47 / 1.30	0.49 / 1.29	0.55 / 1.21
Total fat mass (kg)	M	0.24 / 1.90	0.37 / 1.73	0.27 / 1.87	0.30 / 1.83
	F	0.33 / 2.43	0.55 / 1.98	0.55 / 2.01	0.61 / 1.87

Table 3.2 shows the mean results obtained from fivefold cross-validation of 3DO body composition models constructed using only the digital anthropometric variables and the PCA scores of all the digital anthropometric measurements. The models using only the anthropometric variables reported R^2 values varying from -0.02 (BF percentage) to 0.88 (total lean mass) for males, while values varying from 0.29 (BF percentage) to 0.69 (total lean mass) for females. The models using the PCA scores of all the anthropometric measurements reported R^2 values ranging from 0.02 (BF percentage) to 0.81 (total lean mass) for males, whereas values ranging from 0.08 (BF percentage) to 0.61 (total lean mass) for females.

Table 3.2: 3DO body composition models from stepwise linear regression to predict DXA total and regional body composition. The mean results from fivefold cross-validation are reported for the following models from left to right: digital anthropometric variables and PCA scores of all the digital anthropometric measurements.

Outcome	**Sex**	**Model type**	
		Anthropometric variables only	PC of all anthropometric measurements
		R^2 / RMSE	R^2 / RMSE
BF (%)	M	-0.02 / 2.40	0.02 / 2.44
	F	0.29 / 3.24	0.08 / 3.38
Total lean mass (kg)	M	0.88 / 2.72	0.81 / 3.17
	F	0.69 / 1.99	0.61 / 2.37
Appendicular lean soft mass (kg)	M	0.86 / 1.64	0.76 / 2.03
	F	0.62 / 1.30	0.52 / 1.55
Lean soft mass arms (kg)	M	0.73 / 0.66	0.60 / 0.79
	F	0.32 / 0.37	0.46 / 0.36
Lean soft mass legs (kg)	M	0.79 / 1.50	0.72 / 1.61
	F	0.57 / 1.19	0.42 / 1.43
Total fat mass (kg)	M	0.35 / 1.75	0.32 / 1.88
	F	0.58 / 1.95	0.50 / 1.91

Test set

To test the generalization capabilities of the models on unseen data, performance was evaluated on the test set, which remained untouched up to this point. The prediction equations were obtained by multiple linear regression applied to the training set, using variables selected through stepwise regression based on the Bayesian Information Criterion (BIC).

The results from the test set evaluation of 3DO body composition models built using A-pose meshes and PCA scores of the anthropometric measurements are presented in Table 3.3. The A-pose PC-only model showed R^2 values between -0.26 (BF percentage) and 0.75 (total lean mass and appendicular lean soft mass) for males, while values between 0.08 (lean soft mass arms) and 0.54 (total fat mass) for females. The A-pose PC + anthro model reported R^2 values ranging from -0.20 (BF percentage) to 0.91 (total lean mass) for males, and from 0.15 (lean soft mass arms) to 0.48 (total lean mass) for females. The models using the PCA scores of the anthropometric measurements showed R^2 values between -0.17 (BF percentage) to 0.81 (total lean mass) for males, and values between 0.30 (BF percentage) and 0.75 (total lean mass) for females.

Table 3.3: 3DO body composition models from stepwise linear regression to predict DXA total and regional body composition. The results from the test set are reported for the following models from the top to the bottom: PCA scores of the A-pose meshes, PCA scores of the A-pose meshes and anthropometric variables, PCA scores of all the digital anthropometric measurements.

Model	**Outcome**	**Male** R^2 / RMSE	**Female** R^2 / RMSE
A-pose PC-only	BF (%)	-0.26 / 3.48	0.26 / 2.94
	Total lean mass (kg)	0.75 / 3.77	0.31 / 2.60
	Appendicular lean soft mass (kg)	0.75 / 2.26	0.23 / 1.74
	Lean soft mass arms (kg)	0.70 / 0.70	0.08 / 0.45
	Lean soft mass legs (kg)	0.69 / 1.89	0.12 / 1.61
	Total fat mass (kg)	0.02 / 2.35	0.54 / 1.83
A-pose PC + Anthropometric	BF (%)	-0.20 / 3.40	0.39 / 2.68
	Total lean mass (kg)	0.91 / 2.22	0.48 / 2.25
	Appendicular lean soft mass (kg)	0.90 / 1.44	0.33 / 1.62
	Lean soft mass arms (kg)	0.85 / 0.49	0.15 / 0.44
	Lean soft mass legs (kg)	0.85 / 1.31	0.28 / 1.46
	Total fat mass (kg)	-0.06 / 2.45	0.47 / 1.97
PC of all anthropometric measurements	BF (%)	-0.17 / 3.10	0.30 / 3.64
	Total lean mass (kg)	0.81 / 3.53	0.75 / 1.95
	Appendicular lean soft mass (kg)	0.73 / 2.32	0.60 / 1.32
	Lean soft mass arms (kg)	0.59 / 0.79	0.38 / 0.42
	Lean soft mass legs (kg)	0.69 / 1.87	0.54 / 1.21
	Total fat mass (kg)	0.13 / 2.08	0.53 / 2.22

Table 3.4 and Table 3.5 show the results from the test set of 3DO body composition models built using T-pose meshes, as well as the prediction equation for each outcome. The T-pose PC-only model reported R^2 values ranging from -0.17 (BF percentage) to 0.78 (total lean mass) for males, and from 0.28 (lean soft mass arms) to 0.51 (total lean mass) for females. The T-pose PC + anthro model showed R^2 values between -0.13 (BF percentage) and 0.92 (total lean mass) for males, while values between 0.25 (lean soft mass arms) and 0.62 (total lean mass) for females.

Table 3.6 and Table 3.7 show the results from the test set of 3DO body composition models built using only the anthropometric variables, as well as the prediction equation for each outcome. The R^2 values ranged from -0.12 (BF percentage) to 0.91 (total lean mass) for males, and from 0.25 (lean soft mass arms) to 0.60 (total lean mass and total fat mass) for females.

Table 3.4: 3DO body composition models from stepwise linear regression to predict DXA total and regional body composition. The results from the test set are reported for the following models, from left to right, along with the prediction equations: PCA scores of the T-pose meshes and PCA scores of the T-pose meshes and anthropometric variables (part 1).

Sex	**Outcome**	**T-pose PC-only**			**T-pose PC + Anthropometric**		
		Variable	Coefficient	R^2 / RMSE	Variable	Coefficient	R^2 / RMSE
Female	BF (%)	Intercept	24.016	0.33 / 3.30	Intercept	2.7957	0.40 / 3.11
		PC3	-3.7362		PC6	-4.3079	
		PC4	4.9229		PC8	9.2367	
		PC5	-5.8612		thigh circ.	1.7443	
		PC6	-4.8995		forearm circ.	-3.1329	
		PC8	8.1693				
		PC12	-15.568				
Male	BF (%)	Intercept	12.029	-0.17 / 3.36	Intercept	17.206	-0.13 / 3.30
		PC8	4.6319		PC13	-8.3151	
		PC13	-8.4255		fitness index	-0.18905	
Female	Total lean mass (kg)	Intercept	43.255	0.51 / 2.55	Intercept	-13.999	0.62 / 2.24
		PC1	0.47579		PC12	6.7333	
		PC3	-5.9795		height	0.1903	
		PC4	2.1205		weight	0.45318	
		PC5	-3.7218				
Male	Total lean mass (kg)	Intercept	62.1	0.78 / 3.67	Intercept	-48.803	0.92 / 2.19
		PC1	0.99667		MSI	6.3688	
		PC2	1.7922		forearm circ.	5.5873	
		PC3	-2.1235		arm volume	-0.0017886	
		PC4	14.887		surface area leg	0.0022715	
		PC6	-6.8119		upper arm circ.	-1.6816	
		PC7	-7.4366		ankle circ.	-2.0571	
		PC13	10.417		weight	0.57674	
Female	Appendicular lean soft mass (kg)	Intercept	21.007	0.40 / 1.78	Intercept	-10.069	0.45 / 1.72
		PC1	0.25815		PC13	-5.1329	
		PC3	-3.2407		height	0.10391	
		PC4	1.4578		weight	0.24473	
		PC5	-2.0405				
Male	Appendicular lean soft mass (kg)	Intercept	31.952	0.74 / 2.37	Intercept	-5.8867	0.90 / 1.50
		PC1	0.56122		PC1	0.11301	
		PC2	0.84737		PC9	-3.7932	
		PC3	-0.84918		hip circ.	-0.12787	
		PC4	7.7668		thigh circ.	0.6276	
		PC6	-3.0714		arm volume	-0.00060276	
					weight	0.30308	
Female	Lean soft mass arms (kg)	Intercept	4.1106	0.28 / 0.41	Intercept	-0.27359	0.25 / 0.42
		PC1	0.044947		torso volume	0.000057391	
		PC3	-0.69785		surface area leg	0.00029048	
		PC4	0.49311				
		PC5	-0.43218				
Male	Lean soft mass arms (kg)	Intercept	6.8916	0.70 / 0.73	Intercept	-1.6162	0.82 / 0.56
		PC1	0.14048		PC8	-1.5523	
		PC2	0.2885		PC9	-1.1845	
		PC4	2.3292		PC13	2.3289	
		PC5	0.57979		weight	0.12104	
		PC6	-0.86782				
		PC7	-0.97744				
		PC8	-1.4221				
		PC13	3.2288				

Table 3.5: 3DO body composition models from stepwise linear regression to predict DXA total and regional body composition. The results from the test set are reported for the following models, from left to right, along with the prediction equations: PCA scores of the T-pose meshes and PCA scores of the T-pose meshes and anthropometric variables (part 2).

Sex	**Outcome**	**T-pose PC-only**			**T-pose PC + Anthropometric**		
		Variable	Coefficient	R^2 / RMSE	Variable	Coefficient	R^2 / RMSE
Female	Lean soft mass legs (kg)	Intercept	16.898	0.33 / 1.64	Intercept	5.5875	0.39 / 1.56
		PC1	0.21277		PC1	0.099081	
		PC3	-2.5345		weight	0.1988	
		PC5	-1.6245				
Male	Lean soft mass legs (kg)	Intercept	25.069	0.73 / 1.81	Intercept	-19.887	0.86 / 1.31
		PC1	0.42101		PC9	-3.756	
		PC2	0.54317		thigh circ.	0.41206	
		PC3	-0.66322		outside leg length	0.11997	
		PC4	5.4617		arm volume	-0.00049231	
		PC6	-2.2135		weight	0.19486	
Female	Total fat mass (kg)	Intercept	13.758	0.49 / 2.14	Intercept	-9.5093	0.61 / 1.88
		PC1	0.095648		PC8	5.9487	
		PC2	0.46068		thigh circ.	0.98083	
		PC3	-4.7589		forearm circ.	-1.9453	
		PC4	4.473		weight	0.27519	
		PC5	-5.614				
		PC6	-3.9892				
		PC8	6.0805				
		PC12	-10.097				
Male	Total fat mass (kg)	Intercept	8.536	0.08 / 2.37	Intercept	8.4618	0.08 / 2.36
		PC1	0.18206		PC13	-5.8362	
		PC4	2.8618		MSI	-4.1306	
		PC8	3.0935		weight	0.1715	

Table 3.6: 3DO body composition models from stepwise linear regression to predict DXA total and regional body composition. The results from the test set are reported for the digital anthropometric variables model along with the prediction equations (part 1).

Sex	**Outcome**	**Anthropometric variables only**		
		Variable	Coefficient	R^2 / RMSE
Females	BF (%)	Intercept	-1.2731	0.37 / 3.20
		thigh circ.	1.6776	
		forearm circ.	-2.8027	
Males	BF (%)	Intercept	17.215	-0.12 / 3.29
		fitness index	-0.18942	
Females	Total lean mass (kg)	Intercept	-13.91	0.60 / 2.30
		height	0.19273	
		weight	0.44521	
Males	Total lean mass (kg)	Intercept	-32.792	0.91 / 2.38
		hip circ.	-0.16825	
		neck circ.	0.84329	
		arm volume	-0.00052473	
		thigh circ. right	0.70438	
		weight	0.56334	
Females	Appendicular lean soft mass (kg)	Intercept	-9.7961	0.45 / 1.71
		height	0.10136	
		weight	0.24715	
Males	Appendicular lean soft mass (kg)	Intercept	-23.407	0.89 / 1.52
		hip circ.	-0.14961	
		thigh circ.	0.67966	
		arm volume	-0.00064623	
		height	0.096379	
		weight	0.29969	
Females	Lean soft mass arms (kg)	Intercept	-0.27359	0.25 / 0.42
		torso volume	0.000057391	
		surface area leg	0.00029048	
Males	Lean soft mass arms (kg)	Intercept	-1.9302	0.83 / 0.54
		hip circ.	-0.04582	
		arm circ.	0.1026	
		weight	0.11241	

Table 3.7: 3DO body composition models from stepwise linear regression to predict DXA total and regional body composition. The results from the test set are reported for the digital anthropometric variables model along with the prediction equations (part 2).

Sex	**Outcome**	**Anthropometric variables only**		
		Variable	Coefficient	R^2 / RMSE
Females	Lean soft mass legs (kg)	Intercept	-8.5134	
		height	0.086065	0.39 / 1.56
		weight	0.19676	
Males	Lean soft mass legs (kg)	Intercept	-14.453	
		hip circ.	-0.13074	
		thigh circ.	0.53377	
		wrist circ.	2.1209	0.85 / 1.35
		arm volume	-0.00073702	
		ankle circ.	-0.78404	
		weight	0.18867	
Females	Total fat mass (kg)	Intercept	-0.018941	
		thigh circ.	0.69843	
		forearm circ.	-1.2356	0.60 / 1.91
		height	-0.090139	
		weight	0.3472	
Males	Total fat mass (kg)	Intercept	9.1933	
		MSI	-4.3895	0.09 / 2.35
		weight	0.17175	

Chapter 4

Discussion

This chapter discusses the results obtained in this thesis study, which are presented in Chapter 3.

Table 4.1 shows the results obtained from the test set for all types of regression models in terms of R^2 and RMSE.

T-pose PC-only models showed a slight improvement over the A-pose PC-only models for the males, whereas a great improvement for the females, except for the total fat mass estimate. Performance improved further when anthropometric variables were included in the models. T-pose PC + anthro models exhibited very similar performance to A-pose PC + anthro models for the males, whereas they showed a marked improvement for the females. From just two photos, an avatar in A-pose can be obtained, along with its associated digital anthropometry. With minimal pre-processing, performance similar to that of reposed 3DO meshes to a standardized T-pose can be obtained in the male population, especially when constructing hybrid models that incorporate anthropometric variables. In the latter case, the metrics are nearly identical. A substantial difference is seen between the A-pose and T-pose models in the female population, with R^2 values increasing to a 0.2 difference (total lean mass, PC-only models). As demonstrated by Wong et al. [30], more accurate and precise models can be obtained by reposing 3DO meshes to a standardized pose. This is due to the fact that the majority of the variance related to the pose is eliminated, leaving mainly the variance related to the shape. However, in this study, there is a serious limitation. The 2024 A-pose scans were excluded from the dataset because the vertex order of the meshes provided by Size Stream has changed over the years, making it impossible to merge these scans with those from the other two years. This resulted in different sizes of the datasets for A-pose and T-pose avatars, which negatively affected the construction of linear regression models. The smaller the dataset, the worse the performance is expected to be, because there is not enough data to learn from. This limitation is especially evident in the female population, since the year 2024 alone contains 45 observations

Table 4.1: 3DO body composition models from stepwise linear regression to predict DXA total and regional body composition. The results from the test set are reported for all the models. From left to right: PCA scores of the A-pose meshes, PCA scores of the A-pose meshes and anthropometric variables, PCA scores of the T-pose meshes, PCA scores of the T-pose meshes and anthropometric variables, digital anthropometric variables, and PCA scores of all the digital anthropometric measurements.

Outcome	**Sex**	**Model type**					
		A-pose PC-only R^2 / RMSE	A-pose PC + Anthro R^2 / RMSE	T-pose PC-only R^2 / RMSE	T-pose PC + Anthro R^2 / RMSE	Anthro-only R^2 / RMSE	PC-Anthro R^2 / RMSE
BF (%)	M	-0.26 / 3.48	-0.20 / 3.40	-0.17 / 3.36	-0.13 / 3.30	-0.12 / 3.29	-0.17 / 3.10
	F	0.26 / 2.94	0.39 / 2.68	0.33 / 3.30	0.40 / 3.11	0.37 / 3.20	0.30 / 3.64
Total lean mass (kg)	M	0.75 / 3.77	0.91 / 2.22	0.78 / 3.67	0.92 / 2.19	0.91 / 2.38	0.81 / 3.53
	F	0.31 / 2.60	0.48 / 2.25	0.51 / 2.55	0.62 / 2.24	0.60 / 2.30	0.75 / 1.95
App. lean soft mass (kg)	M	0.75 / 2.26	0.90 / 1.44	0.74 / 2.37	0.90 / 1.50	0.89 / 1.52	0.73 / 2.32
	F	0.23 / 1.74	0.33 / 1.62	0.40 / 1.78	0.45 / 1.72	0.45 / 1.71	0.60 / 1.32
Lean soft mass arms (kg)	M	0.70 / 0.70	0.85 / 0.49	0.70 / 0.73	0.82 / 0.56	0.83 / 0.54	0.59 / 0.79
	F	0.08 / 0.45	0.15 / 0.44	0.28 / 0.41	0.25 / 0.42	0.25 / 0.42	0.38 / 0.42
Lean soft mass legs (kg)	M	0.69 / 1.89	0.85 / 1.31	0.73 / 1.81	0.86 / 1.31	0.85 / 1.35	0.69 / 1.87
	F	0.12 / 1.61	0.28 / 1.46	0.33 / 1.64	0.39 / 1.56	0.39 / 1.56	0.54 / 1.21
Total fat mass (kg)	M	0.02 / 2.35	-0.06 / 2.45	0.08 / 2.37	0.08 / 2.36	0.09 / 2.35	0.13 / 2.08
	F	0.54 / 1.83	0.47 / 1.97	0.49 / 2.14	0.61 / 1.88	0.60 / 1.91	0.53 / 2.22

out of a total of 156, resulting in nearly one third fewer data points for building A-pose models. This largely explains the significant improvement in performance when using T-pose models instead of A-pose ones. Yet, it prevents a full analysis of the contribution due to the elimination of the pose-related variance. In the male population, the missing year in the A-pose dataset is not a major problem since only 15 observations out of 262 are lost, preserving the dataset's size. In light of the problems experienced with raw scans, one of the many advantages of using Meshcapade is highlighted: it standardizes the meshes, avoiding problems due to the order of the vertices. In fact, the avatars in T-pose did not report any issue.

The performance of anthro-only male models was comparable to that of A-pose and T-pose PC + anthro models, and they outperformed PC-only models. Similarly, anthro-only female models exhibited performance that was identical or nearly identical to that of T-pose PC + anthro models. Their performance was equal in the estimation of appendicular lean soft mass (R^2 of 0.45 and RMSE of 1.72 and 1.71), lean soft mass arms (R^2 of 0.25 and RMSE of 0.42), and lean soft mass legs (R^2 of 0.39 and RMSE of 1.56). They also outperformed PC-only models, except for lean soft mass arms (R^2 of 0.25 for the anthro-only model, and R^2 of 0.28 for the T-pose PC-only model). For this population of young soccer players, models using only digital anthropometric measurements, from a set of 26 variables selected from all those provided by Size Stream, have shown

to be equally or more predictive than models that use advanced statistical shape modeling, such as PCA, to capture complex shape features. This result may reflect the relatively homogeneous body shape and composition typical of young athletes, where anthropometric measurements already capture the main sources of variability.

The anthropometric variables most frequently selected by stepwise regression for the T-pose PC + anthro models were weight, height, thigh circumference, forearm circumference, and arm volume; while for the anthro-only models, the selected variables were weight, height, thigh circumference, arm volume, and hip circumference. In both T-pose PC + anthro and anthro-only models, arm volume appeared exclusively in the prediction equations for male lean mass, while hip circumference appeared exclusively in the equations for male lean mass of the anthro-only models. The other variables appeared as predictors in both lean and fat mass equations. These results suggest that, in the case of young male athletes, arm volume and hip circumference are strong predictors of lean mass, highlighting the importance of specific regional measurements alongside more general indices like weight and height.

The models used to estimate BF percentage (Figure 4.1) reported R^2 values ranging from 0.26 (A-pose PC-only) to 0.4 (T-pose PC + anthro) for females, and from -0.26 (A-pose PC-only) to -0.12 (Anthro-only) for males.

For total lean mass (Figure 4.2), R^2 scores ranged between 0.31 (A-pose PC-only) and 0.75 (PC-anthro) in females, and between 0.75 (A-pose PC-only) and 0.92 (T-pose PC + anthro) in males.

For appendicular lean soft mass (Figure 4.3), R^2 values varied from 0.23 (A-pose PC-only) to 0.6 (PC-anthro) for females, and 0.73 (PC-anthro) to 0.9 (A-pose PC and T-pose PC + anthro) for males.

For lean soft mass arms (Figure 4.4) reported R^2 values ranging from 0.08 (A-pose PC-only) to 0.38 (PC-anthro) for females, and from 0.59 (PC-anthro) to 0.85 (A-pose PC + anthro) for males.

For lean soft mass legs (Figure 4.5), R^2 scores ranged between 0.12 (A-pose PC-only) and 0.54 (PC-anthro) in females, and between 0.69 (A-pose PC-only and PC-anthro) and 0.86 (T-pose PC + anthro) in males.

When estimating total fat mass (Figure 4.6), R^2 values varied from 0.47 (A-pose PC + anthro) to 0.61 (T-pose PC + anthro) for females, and -0.06 (A-pose PC + anthro) to 0.13 (PC-anthro) for males.

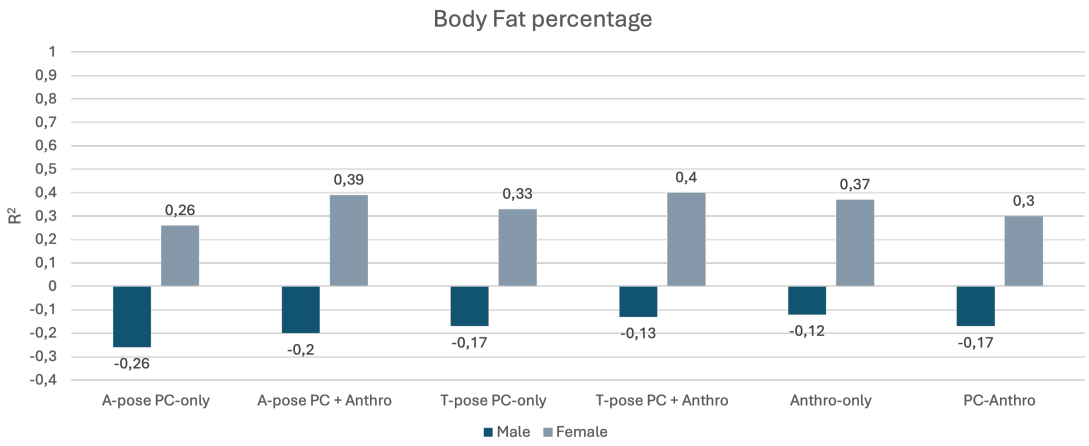

Figure 4.1: Comparison of R^2 values obtained using the regression models to estimate BF percentage for the male and female test sets.

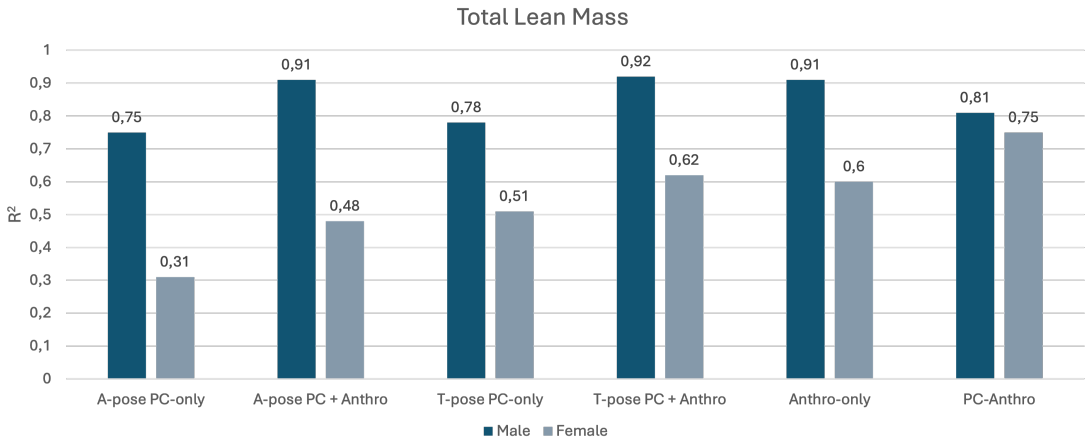

Figure 4.2: Comparison of R^2 values obtained using the regression models to estimate total lean mass for the male and female test sets.

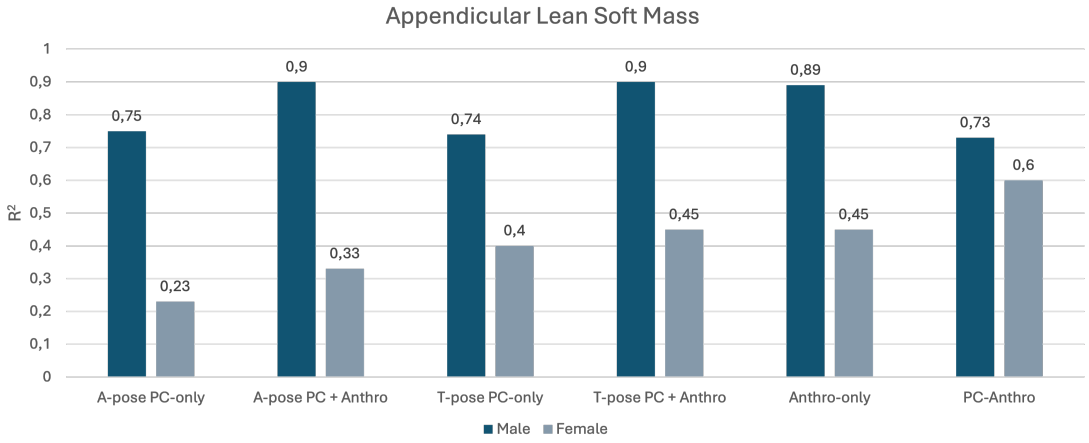

Figure 4.3: Comparison of R^2 values obtained using the regression models to estimate appendicular lean soft mass for the male and female test sets.

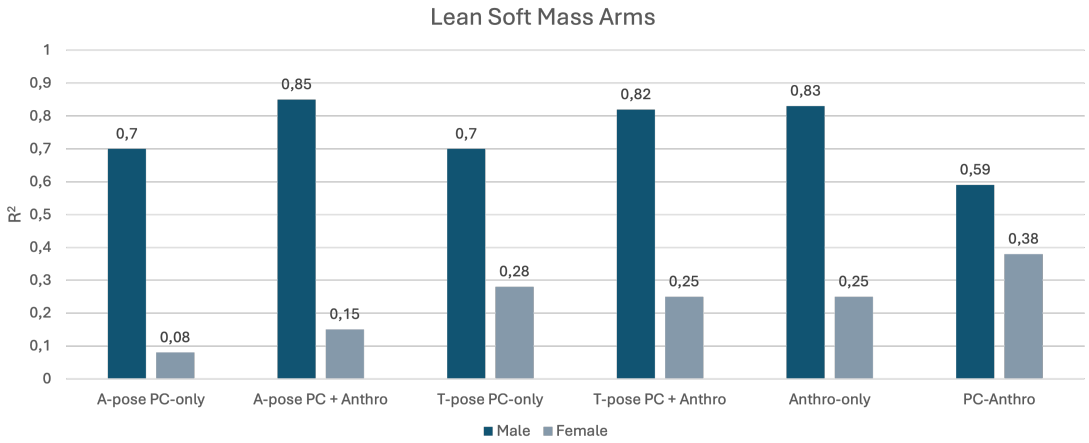

Figure 4.4: Comparison of R^2 values obtained using the regression models to estimate lean soft mass arms for the male and female test sets.

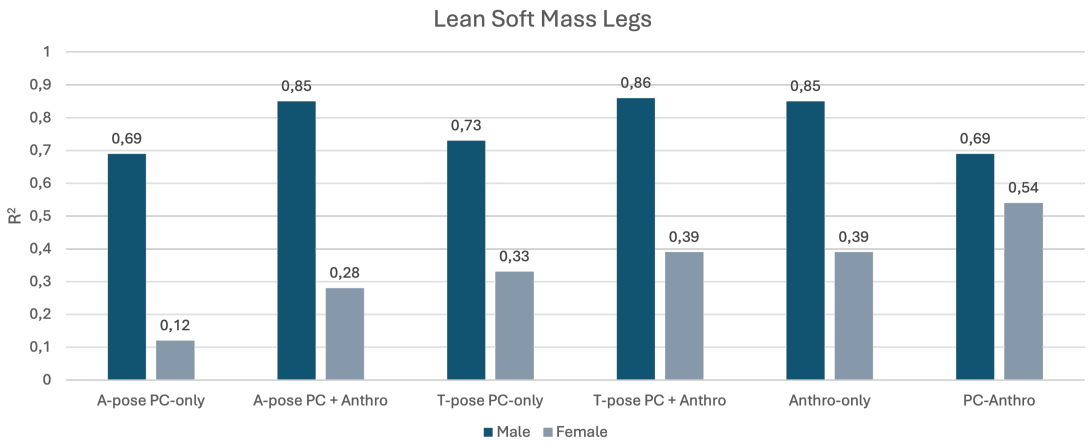

Figure 4.5: Comparison of R^2 values obtained using the regression models to estimate lean soft mass legs for the male and female test sets.

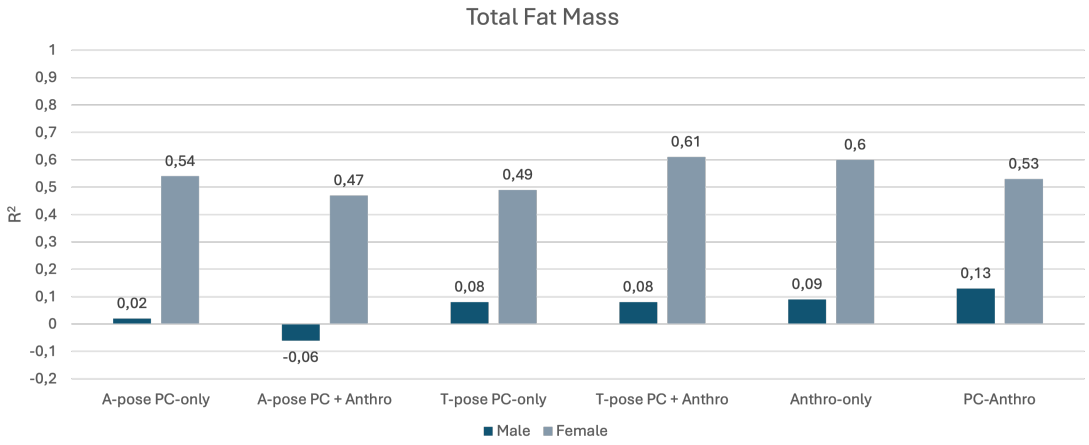

Figure 4.6: Comparison of R^2 values obtained using the regression models to estimate total fat mass for the male and female test sets.

In light of these results, the following can be stated:

- Estimates of fat mass were inaccurate in the male population since R^2 values close to or even below 0 are recorded. Negative R^2 values indicate that the regression model performs worse than simply predicting the mean value of the outcome for all subjects. In contrast, estimates of total and regional lean mass were extremely accurate. R^2 values as high as 0.92 are recorded. The A-pose PC + anthro, T-pose PC + anthro, and anthro-only models accurately and precisely predicted these outcomes.
- No female model for total and regional lean mass prediction reported performance as accurate and precise as male models. However, when it comes to predicting fat mass outcomes, the performance was considerably better than that of the male models. Interestingly, the PC-anthro models, created for exploratory purposes and as a possible direction for future development, reported the best performance in estimating lean mass outcomes. The improvement in R^2 was significant compared to the other models.

In the case of young, lean, trained male athletes, automated anthropometry and body shape-related features, captured by PCA, are insufficient and inadequate predictors for estimating body fat percentage and total fat mass. As presented in Section 2.3.2, in Figure 2.14 and Figure 2.15, the PCs are poorly correlated, if uncorrelated at all, with the two fat mass outcomes. Similarly, Figure 2.19 shows that body fat percentage is uncorrelated with almost all anthropometric variables. Where there is correlation, it is extremely low. These findings suggest that, due to the relatively homogeneous body composition of the participants, there were no variables that could explain fat mass, which resulted in poor model performance.

Leaving aside PC-anthro models, which as has been noted, performed well with female lean mass estimates, the most accurate models are those that use anthropometric variables for their constructions, whether they are hybrid PC + anthro or anthro-only models. This demonstrates that PCs alone are insufficient for estimating DXA-derived total and regional body composition in youth soccer players; digital anthropometric measurements are recommended in conjunction with PCs, if not alone. This approach allows to take full advantage of the potential offered by 3DO imaging systems.

This study has its limitations. First, all scans from 2024 had to be excluded from the analysis of A-pose avatars, due to a change in the vertex order of the meshes, that made them incompatible with those from previous years. This led to a difference in the number of observations in the A-pose and T-pose datasets, which affects the comparability of the results. Second, the study sample is extremely homogeneous because it consists only of young athletes. This homogeneity may limit the ability of PCA to capture body shape variance. This is reflected by the

fact that few PCs explain more than 95% of the total variance in the dataset. An extreme case is seen in the T-pose avatars, where the first PC alone explains more than 95% of the shape variance. Lastly, the models were built using data generated by a specific application, Mobile Fit. This may limit the applicability of the results to other scanning technologies.

Chapter 5

Conclusions

The aim of this thesis is the prediction of body composition, total and regional, derived from DXA in a population of young soccer players, through the use of principal component analysis (PCA) on raw and reposed 3DO whole-body scans. The results showed that estimates of lean mass, total and regional, were highly accurate in male athletes, with R^2 values as high as 0.92 (total lean mass). This level of accuracy was achieved with both hybrid models that combined principal components (PCs) and anthropometry, and models that used only anthropometric measurements. In contrast, estimates of fat mass were inaccurate since they reported R^2 values near or below 0. In females, none of the models achieved high performance in lean mass prediction, and fat mass estimates achieved moderate accuracy. In light of these results, the thesis's goal was only partially achieved, since accurate performance was reached for specific outcomes and subgroups. In a population of young athletes, their homogeneous body shape and composition may limit the ability of PCA to capture body shape variance. In fact, models that used only digital anthropometric measurements have shown to be equally or more precise than models that used PCA to capture complex shape features. The promising results observed when using PC-anthro models to predict lean mass in female athletes suggest a possible direction for future investigations. Future work should validate these approaches using larger, more heterogeneous populations, including different sports and age groups. Additionally, the applicability of these models to other 3DO imaging systems should be assessed. In conclusion, this study shows the potential and current limitations of 3DO body composition estimation in young athletes, highlighting the necessity of further research to develop more reliable and accurate models for monitoring body composition in youth sports settings.

Appendix A

Mathematical Formulation of PCA

This appendix provides the mathematical background of the principal component analysis (PCA), based on the lecture slides by Grosso [57].

PCA is a linear dimensionality reduction method used for exploratory data analysis, visualization and data pre-processing.

Working with large amounts of data can present a number of challenges:

- Useful information is often hidden among hundreds or thousands of variables (size of the data).
- Measurements are often highly correlated with each other. The number of independent variables is significantly smaller than the number of measurements available.
- Noise in the measurements.

PCA allows for an interpretation based on all variables simultaneously, providing a deeper understanding than looking at the individual variables alone.

The goal of PCA is to transform the original variables, which are high dimensional, and strongly correlated, into a new set of artificial, independent variables with a much lower dimension, known as principal components (PCs).

The data must be collected on a matrix $\mathbf{X}$ of size $\mathbf{I} \times \mathbf{J}$, where the columns ($\mathbf{J}$) represent the variables and the rows ($\mathbf{I}$) represent the observations.

Before applying PCA, the data must undergo mean centering. This process involves subtracting the mean of each column from the corresponding values, as shown in Equation (A.1).

$$x_{ij} = x^*_{ij} - \bar{x}^*_{\cdot j} \quad \text{where} \quad \bar{x}^*_{\cdot j} = \frac{1}{I}\sum_{i=1}^{I} x^*_{ij} \tag{A.1}$$

This leads to a new matrix $\mathbf{X}$, where each column has zero mean:

$$\mathbf{X} = \begin{bmatrix} x^*_{11} - \bar{x}^*_{\cdot 1} & \cdots & x^*_{1J} - \bar{x}^*_{\cdot J} \\ \vdots & \ddots & \vdots \\ x^*_{I1} - \bar{x}^*_{\cdot 1} & \cdots & x^*_{IJ} - \bar{x}^*_{\cdot J} \end{bmatrix}$$

Mean centering allows for the consideration of the covariance matrix:

$$\mathbf{C} = \mathbf{X}^{\mathrm{T}}\mathbf{X} \tag{A.2}$$

For any element $\mathbf{C}_{kl}$, this corresponds to the following scalar product:

$$\mathbf{C}_{kl} = (\mathbf{X}^{\mathrm{T}}\mathbf{X})_{kl} = \sum_{i=1}^{I} x_{ik}\, x_{il} \tag{A.3}$$

In particular, the diagonal elements of $\mathbf{C}$ express the total variance of the j-th variable.

$$\mathbf{C}_{jj} = (\mathbf{X}^{\mathrm{T}}\mathbf{X})_{jj} = \sum_{i=1}^{I} x_{ij}^2 \tag{A.4}$$

PCA is based on the decomposition of the dataset matrix $\mathbf{X}$:

$$\mathbf{X} = \mathbf{T} \cdot \mathbf{P}^{\mathrm{T}} \tag{A.5}$$

where $\mathbf{T}$ is the scores matrix, containing the artificial variables generated by PCA, and $\mathbf{P}$ is the loadings matrix, the rotation matrix that relates the artificial variables to the original ones.

The PCA decomposition exhibits several important mathematical properties:

1. The resulting scores matrix $\mathbf{T}$ is mean centered, just as the original data matrix $\mathbf{X}$. This implies that the mean of each column is zero

$$\bar{x}_{\cdot j} = 0 \quad \forall j = 1, \ldots, J \quad \Rightarrow \quad \bar{t}_{\cdot j} = 0 \quad \forall j = 1, \ldots, J \tag{A.6}$$

2. The column vectors of the scores matrix $\mathbf{T}$ are orthogonal:

$$\mathbf{t}_m^{\mathrm{T}}\mathbf{t}_n = 0 \quad \forall m \neq n \tag{A.7}$$

Consequently, the matrix $\mathbf{\Lambda} = \mathbf{T}^{\mathrm{T}} \cdot \mathbf{T}$ is diagonal.

3. The loadings matrix $\mathbf{P}$ is orthogonal:

$$\mathbf{P}^{\mathrm{T}} = \mathbf{P}^{-1} \quad \Rightarrow \quad \mathbf{P}^{\mathrm{T}} \cdot \mathbf{P} = \mathbf{I} \tag{A.8}$$

The PCA scores and loadings can be related to the calculation of the eigenvalues and eigenvectors of the covariance matrix $\mathbf{C}$. Since $\mathbf{C}$ is a square and symmetrical matrix, all eigenvalues are real and positive, and all eigenvectors are orthogonal to each other.

Starting from the PCA decomposition of the dataset matrix $\mathbf{X} = \mathbf{T} \cdot \mathbf{P}^{\mathrm{T}}$, one can derive the following relationships:

$$\mathbf{C} = \mathbf{X}^{\mathrm{T}} \cdot \mathbf{X} = \mathbf{P} \cdot \mathbf{T}^{\mathrm{T}} \cdot \mathbf{T} \cdot \mathbf{P}^{\mathrm{T}} = \mathbf{P} \cdot \mathbf{\Lambda} \cdot \mathbf{P}^{\mathrm{T}} = \mathbf{P} \cdot \mathbf{\Lambda} \cdot \mathbf{P}^{-1} \tag{A.9}$$

This equation corresponds to the eigendecomposition of the square matrix $\mathbf{C}$. In this context:

- $\mathbf{\Lambda}$ is a diagonal matrix whose diagonal elements are the eigenvalues of $\mathbf{C}$.
- The m-th element, $\mathbf{t}_m^{\mathrm{T}}\mathbf{t}_m = \mathbf{\Lambda}_{mm}$, represents the variance explained by the m-th score.
- $\mathbf{P}$ is a $n \times n$ square matrix whose columns are the eigenvectors of the covariance matrix $\mathbf{C}$. Its m-th column, p_m, represents the direction of the m-th principal component of the data contained in the original matrix $\mathbf{X}$.

The eigenvectors, p_m, obtained can be used to calculate the corresponding scores through the following relation:

$$\mathbf{X} = \mathbf{T} \cdot \mathbf{P}^{\mathrm{T}} \;\Rightarrow\; \mathbf{X} \cdot \mathbf{P} = \mathbf{T} \cdot \mathbf{P}^{\mathrm{T}} \cdot \mathbf{P} \;\Rightarrow\; \mathbf{T} = \mathbf{X} \cdot \mathbf{P} \tag{A.10}$$

The original variables are projected onto the orthogonal space defined by the eigenvectors/loadings.

The eigenvalues of the covariance matrix are directly related to the variance explained by each score:

$$\lambda_j = \mathbf{t}_j^{\mathrm{T}}\mathbf{t}_j = \sum_{i=1}^{I} t_{i,j}^2 \tag{A.11}$$

The $\mathbf{T}$ matrix preserves the total variance present in the original dataset.

The eigenvectors are typically ordered by their corresponding eigenvalue size (variance) in descending order. This ensures that the first columns of the $\mathbf{P}$ matrix (the first PCs) represent the directions along which the variance in the original data is maximized. Therefore, the first PCs explain most of the original variance.

By selecting only the first columns of $\mathbf{T}$, it is possible to effectively represent most of the information contained in the original data, resulting in a significant reduction in dimensionality.

Appendix B

PCA on Anthropometric Measurements

In addition to the PCA performed on the male and female datasets of the avatars, a second analysis was conducted using the anthropometric measurements provided by Size Stream. The objective was to evaluate their predictive power in relation to the DXA variables. This appendix describes the specific procedure followed to apply PCA to the full set of 242 anthropometric measurements contained in the `Core Measures Metric.csv` file. The analysis pipeline was similar to the one previously applied to the three-dimensional meshes, as shown in Figure B.1. First, the dimensionality was reduced via PCA; then, the resulting PCs were used as input for the construction of multiple linear regression models. Similar to the previous analysis, the three year datasets (2022, 2023, and 2024) were processed individually.

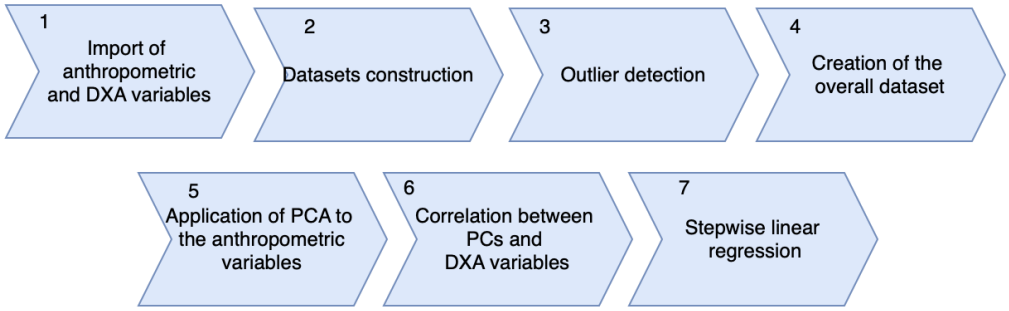

Figure B.1: Schematic representation of the data processing and analysis pipeline for the PCA performed on the anthropometric measurements.

For each subject, the `Core Measures Metric.csv` file was imported into `MATLAB`. Then, all 242 anthropometric measurements were selected and saved in separate matrices for males and females. Files containing the DXA outputs were also imported into `MATLAB`, and the same variables reported in Section 2.2.3 were calculated and extracted. At this point, since there were available two 3DO scans and, consequently, two `Core Measures Metric.csv` files for each individual, it was necessary to create a dataset with a single observation per subject. For this purpose, the anthropometric variables extracted from the CSV files were averaged. As a result, each subject was represented by a single row of anthropometric measurements, and the corresponding DXA variables. The final pre-processing step was outlier detection, which was performed using Grubbs's test on the values of the anthropometric and DXA variables. Table B.1 shows the number of observation remaining after outlier detection.

Once the pre-processing was done separately for the three years, the three datasets were merged so that the overall dataset could be obtained. This final dataset consists of 249 male observations and 136 female observations. Subsequently, PCA was applied to the anthropometric measurements. Figure B.2 shows that more than 95% of the total variance is explained by the first PC in both male and female datasets. To evaluate the relationship between the PCs and the DXA variables, Pearson's correlation coefficients were calculated. The first seven PCs were correlated with all DXA variables. The resulting correlation matrix was visualized as a heatmap. Only statistically significant correlations were maintained (P value < 0.05), while non significant values were replaced with NaN. PC1 was significantly correlated with all DXA variables in both male and female datasets (Figure B.3).

The multiple linear regression models were developed using the same methodology as the PCA of the avatars. Therefore, the details are not reiterated.

The results are reported along with the other models.

Table B.1: Number of observations remaining after outlier detection by year and sex.

Year	Male observation	Female observation
2022	113	53
2023	121	39
2024	15	44

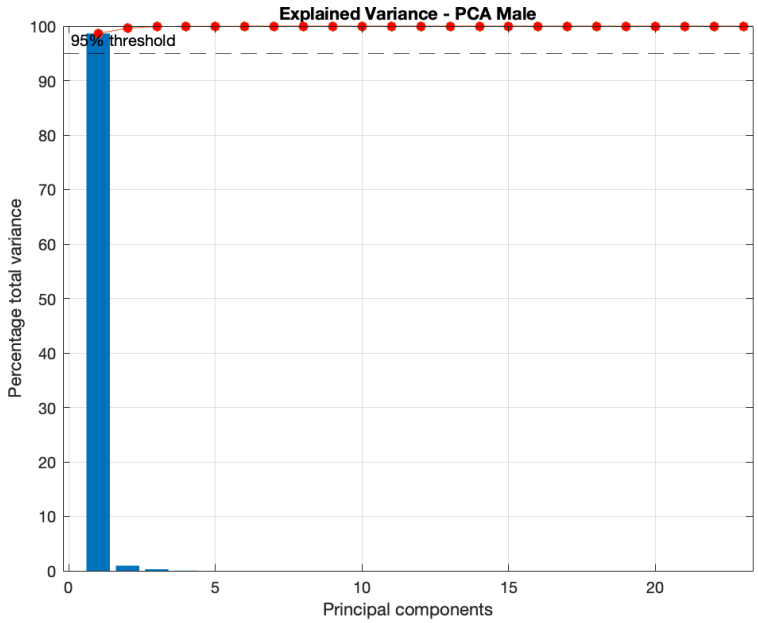

(a) Explained variance – Male

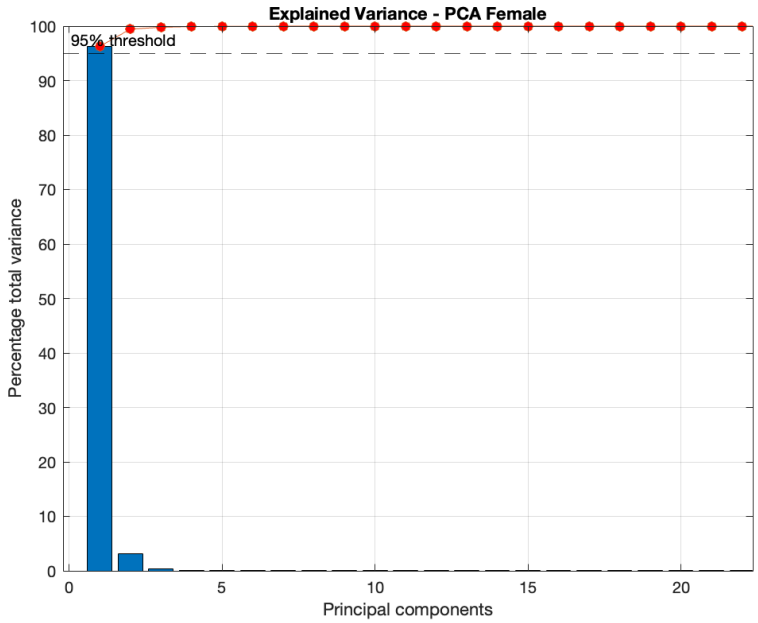

(b) Explained variance – Female

Figure B.2: Percentage of total variance explained by each PC for male (a) and female (b) datasets.

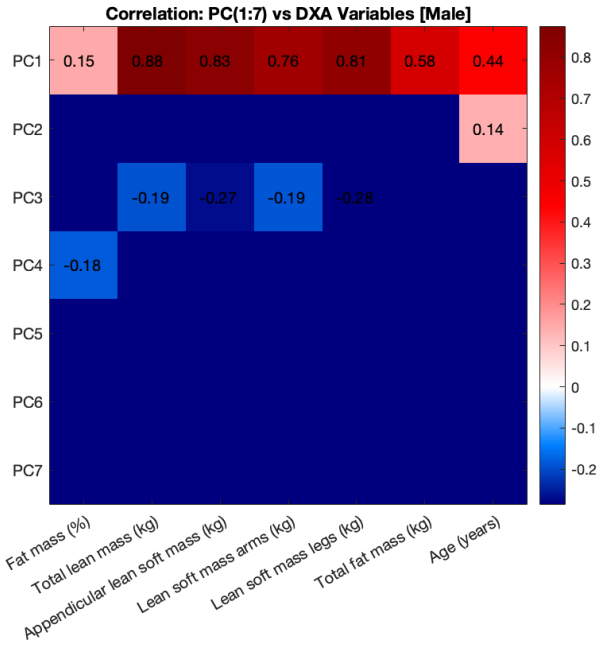

(a) Correlation matrix – Male

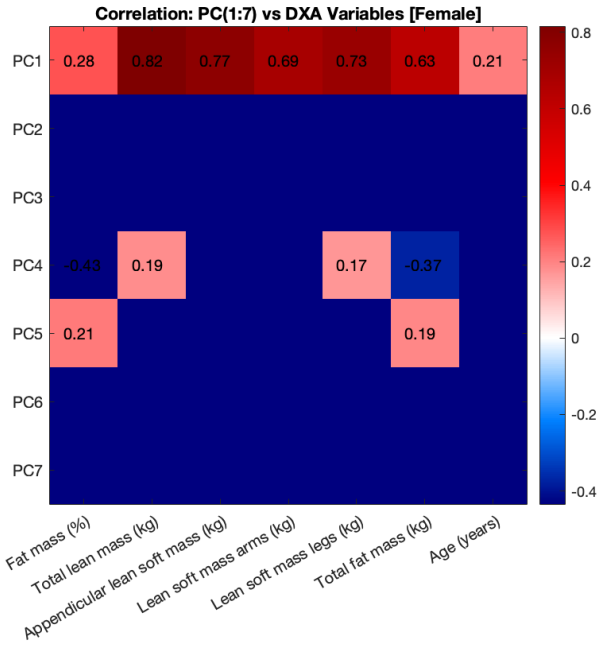

(b) Correlation matrix – Female

Figure B.3: Correlation matrix between PCs and DXA variables for male (a) and female (b) datasets.

Bibliography

[1] Sarah Messiah. «Body Composition». In: *Encyclopedia of Behavioral Medicine*. Ed. by M. D. Gellman. Springer, Cham, 2020, pp. 276–278 (cit. on p. 1).

[2] Marco A. Minetto, Chiara Busso, Andrea Ferraris, Angelo Pietrobelli, John A. Shepherd, Cassidy McCarthy, and Steven B. Heymsfield. «Clinical Anthropometrics and Body Composition from 3-Dimensional Optical Imaging». In: *Journal of Visualized Experiments* 208 (2024) (cit. on pp. 1, 24).

[3] Jonathan P. Bennett et al. «Assessment of clinical measures of total and regional body composition from a commercial 3-dimensional optical body scanner». In: *Clinical Nutrition* 41.1 (2022), pp. 211–218 (cit. on pp. 1, 2, 18).

[4] Kathleen Y. Wolin, Kenneth Carson, and Graham A. Colditz. «Obesity and cancer». In: *The Oncologist* 15.6 (2010), pp. 556–565 (cit. on p. 1).

[5] Jean-Pierre Després. «Body fat distribution and risk of cardiovascular disease: an update». In: *Circulation* 126.10 (2012), pp. 1301–1313 (cit. on p. 1).

[6] Asnawi Abdullah, Johannes Stoelwinder, Susan Shortreed, Rory Wolfe, Christopher Stevenson, Helen Walls, Maximilian de Courten, and Anna Peeters. «The duration of obesity and the risk of type 2 diabetes». In: *Public Health Nutrition* 14.1 (2011), pp. 119–126 (cit. on p. 1).

[7] Leigh C. Ward. «Human body composition: yesterday, today, and tomorrow». In: *European Journal of Clinical Nutrition* 72 (2018), pp. 1201–1207 (cit. on p. 1).

[8] J. A. Batsis, T. A. Mackenzie, L. K. Barre, F. Lopez-Jimenez, and S. J. Bartels. «Sarcopenia, sarcopenic obesity and mortality in older adults: results from the National Health and Nutrition Examination Survey III». In: *European Journal of Clinical Nutrition* 68 (2014), pp. 1001–1007 (cit. on p. 1).

[9] T. Cederholm et al. «GLIM criteria for the diagnosis of malnutrition - A consensus report from the global clinical nutrition community». In: *Journal of Cachexia, Sarcopenia and Muscle* 10.1 (2019), pp. 207–217 (cit. on p. 1).

[10] Michael C. Wong et al. «Children and Adolescents' Anthropometrics Body Composition from 3-D Optical Surface Scans». In: *Obesity (Silver Spring)* 27.11 (2019), pp. 1738–1749 (cit. on pp. 1, 3, 18).

[11] W. M. Verduin, R. Van Den Helder, H. J. Doodeman, E. Struijf, and A. P. J. Houdijk. «Dexa Body Composition Assessment in 10-11 Year Healthy Children». In: *PLOS ONE* 11.10 (2016) (cit. on p. 1).

[12] Mark J. Johnson and R. Mark Beattie. «Making body composition measurement a part of routine care in children». In: *Clinical Nutrition* 37.3 (2018), pp. 763–764 (cit. on p. 1).

[13] Marco A. Minetto et al. «Equations for smartphone prediction of adiposity and appendicular lean mass in youth soccer players». In: *Scientific Reports* 13.20734 (2023) (cit. on pp. 1, 15, 21, 25, 28).

[14] J. E. Morley, R. N. Baumgartner, R. Roubenoff, J. Mayer, and K. S. Nair. «Sarcopenia». In: *Journal of Laboratory and Clinical Medicine* 137.4 (2001), pp. 231–243 (cit. on p. 2).

[15] Cuilin Zhang, Kathryn M. Rexrode, Rob M. van Dam, Tricia Y. Li, and Frank B. Hu. «Abdominal obesity and the risk of all-cause, cardiovascular, and cancer mortality: sixteen years of follow-up in US women». In: *Circulation* 117.13 (2008), pp. 1658–1667 (cit. on p. 2).

[16] Jonathan P. Bennett et al. «Three-dimensional optical body shape and features improve prediction of metabolic disease risk in a diverse sample of adults». In: *Obesity (Silver Spring)* 30.8 (2022), pp. 1589–1598 (cit. on p. 2).

[17] Shohinee Sarma, Sanjeev Sockalingam, and Satya Dash. «Obesity as a multisystem disease: Trends in obesity rates and obesity-related complications». In: *Diabetes, Obesity and Metabolism* 23.Suppl 1 (2021), pp. 3–16 (cit. on p. 2).

[18] Peter T. Katzmarzyk, Ian Janssen, Robert Ross, Timothy S. Church, and Steven N. Blair. «The importance of waist circumference in the definition of metabolic syndrome: prospective analyses of mortality in men». In: *Diabetes Care* 29.2 (2006), pp. 404–409 (cit. on p. 2).

[19] Eric J. Jacobs, Christina C. Newton, Yiting Wang, Alpa V. Patel, Marjorie L. McCullough, Peter T. Campbell, Michael J. Thun, and Susan M. Gapstur. «Waist circumference and all-cause mortality in a large US cohort». In: *Archives of Internal Medicine* 170.15 (2010), pp. 1293–1301 (cit. on p. 2).

[20] Jennifer L. Kuk, Peter T. Katzmarzyk, Milton Z. Nichaman, Timothy S. Church, Steven N. Blair, and Robert Ross. «Visceral fat is an independent predictor of all-cause mortality in men». In: *Obesity (Silver Spring)* 14.2 (2006), pp. 336–341 (cit. on p. 2).

[21] Gill M. Price, Ricardo Uauy, Elizabeth Breeze, Christopher J. Bulpitt, and Astrid E. Fletcher. «Weight, shape, and mortality risk in older persons: elevated waist-hip ratio, not high body mass index, is associated with a greater risk of death». In: *The American Journal of Clinical Nutrition* 84.2 (2006), pp. 449–460 (cit. on p. 2).

[22] Bennett K. Ng et al. «Detailed 3-dimensional body shape features predict body composition, blood metabolites, and functional strength: the Shape Up! studies». In: *The American Journal of Clinical Nutrition* 110.6 (2019), pp. 1316–1326 (cit. on pp. 2, 19).

[23] H. C. Lukaski. «Methods for the assessment of human body composition: traditional and new». In: *The American Journal of Clinical Nutrition* 46.4 (1987), pp. 537–556 (cit. on p. 2).

[24] Isaac Y. Tian et al. «Automated body composition estimation from device-agnostic 3D optical scans in pediatric populations». In: *Clinical Nutrition* 42.9 (2023), pp. 1619–1630 (cit. on pp. 2, 19).

[25] Yao Lu, James K. Hahn, and Xiaoke Zhang. «3D Shape-Based Body Composition Inference Model Using a Bayesian Network». In: *IEEE Journal of Biomedical and Health Informatics* 24.1 (2020), pp. 205–213 (cit. on p. 2).

[26] John A. Shepherd, Bennett K. Ng, Markus J. Sommer, and Steven B. Heymsfield. «Body composition by DXA». In: *Bone* 104 (2017), pp. 101–105 (cit. on p. 2).

[27] Andrea K. Garber et al. «Cross-sectional assessment of body composition and detection of malnutrition risk in participants with low body mass index and eating disorders using 3D optical surface scans». In: *The American Journal of Clinical Nutrition* 118.4 (2023), pp. 812–821 (cit. on p. 2).

[28] M. A. McCrory, T. D. Gomez, E. M. Bernauer, and P. A. Molé. «Evaluation of a new air displacement plethysmograph for measuring human body composition». In: *Medicine & Science in Sports & Exercise* 27.12 (1995), pp. 1686–1691 (cit. on p. 2).

[29] M. Abu Khaled, M. J. McCutcheon, S. Reddy, P. L. Pearman, G. R. Hunter, and R. L. Weinsier. «Electrical impedance in assessing human body composition: the BIA method». In: *The American Journal of Clinical Nutrition* 47.5 (1988), pp. 789–792 (cit. on p. 2).

[30] Michael C. Wong et al. «A pose-independent method for accurate and precise body composition from 3D optical scans». In: *Obesity (Silver Spring)* 29.11 (2021), pp. 1835–1847 (cit. on pp. 3, 19, 31, 59).

[31] Michael C. Wong et al. «Accuracy and Precision of 3-dimensional Optical Imaging for Body Composition by Age, BMI, and Ethnicity». In: *The American Journal of Clinical Nutrition* 118.3 (2023), pp. 657–671 (cit. on pp. 3, 19).

[32] Angelo Pietrobelli, Carmelo Formica, Zimian Wang, and Steven B. Heymsfield. «Dual-energy X-ray absorptiometry body composition model: review of physical concepts». In: *American Journal of Physiology* 271.6 Pt 1 (1996), E941–E951 (cit. on pp. 3, 6).

[33] Caresmed. *Lunar iDXA per la salute delle ossa e metabolica*. Accessed: 2025-05-29. 2025. URL: https://lunar.caresmed.it/gamma/lunar-idxa-per-la-salute-delle-ossa-e-metabolica/ (cit. on p. 3).

[34] Carmelo Messina, Domenico Albano, Salvatore Gitto, Laura Tofanelli, Alberto Bazzocchi, Fabio Massimo Ulivieri, Giuseppe Guglielmi, and Luca Maria Sconfienza. «Body composition with dual energy X-ray absorptiometry: from basics to new tools». In: *Quantitative Imaging in Medicine and Surgery* 10.8 (2020), pp. 1687–1698 (cit. on p. 4).

[35] Steven B. Heymsfield, Brianna Bourgeois, Bennett K. Ng, Markus J. Sommer, Xin Li, and John A. Shepherd. «Digital anthropometry: a critical review». In: *European Journal of Clinical Nutrition* 72.5 (2018), pp. 680–687 (cit. on pp. 7, 12, 13, 17).

[36] Kristijan Bartol, David Bojanić, Tomislav Petković, and Tomislav Pribanić. «A Review of Body Measurement Using 3D Scanning». In: *IEEE Access* 9 (2021), pp. 67281–67301 (cit. on pp. 7–12).

[37] Alice May Bullas, Rebecca Greenwood, Michael Thelwell, and Simon Choppin. «A Review of Commercially Available 3D Surface Imaging Systems for Body Composition Estimation». In: *Applied Sciences* 12.17 (2022), p. 8815 (cit. on pp. 14–16).

[38] Inc. Fit3D. *Fit3D ProScanner*. Accessed: 2025-06-05. 2025. URL: https://www.fit3d.com/3d-body-scanner (cit. on p. 15).

[39] LLC Size Stream. *Mobile Fit Booth Technology*. Accessed: 2025-06-02. 2025. URL: https://www.sizestream.com/technology/mobile-fit-booth (cit. on p. 15).

[40] LLC Size Stream. *Technology Overview*. Accessed: 2025-06-02. 2025. URL: https://www.sizestream.com/technology (cit. on p. 15).

[41] LLC Size Stream. *Mobile Fit FAQ*. Accessed: 2025-06-02. 2025. URL: https://www.sizestream.com/faq-mobile-fit (cit. on p. 15).

[42] B. K. Ng, B. J. Hinton, B. Fan, A. M. Kanaya, and J. A. Shepherd. «Clinical anthropometrics and body composition from 3D whole-body surface scans». In: *European Journal of Clinical Nutrition* 70.11 (2016), pp. 1265–1270 (cit. on p. 18).

[43] Yao Lu, Scott McQuade, and James K. Hahn. «3D Shape-based Body Composition Prediction Model Using Machine Learning». In: *2018 40th Annual International Conference of the IEEE Engineering in Medicine and Biology Society (EMBC)*. Honolulu, HI, USA, July 2018, pp. 3999–4002 (cit. on p. 19).

[44] Sima Sobhiyeh, Nathan Borel, Marcelline Dechenaud, Clinten A. Graham, Michael Wong, Peter Wolenski, John Shepherd, and Steven B. Heymsfield. «Fully Automated Pipeline for Body Composition Estimation from 3D Optical Scans using Principal Component Analysis: A Shape Up Study». In: *2020 42nd Annual International Conference of the IEEE Engineering in Medicine Biology Society (EMBC)*. Montreal, QC, Canada, July 2020, pp. 1853–1858 (cit. on p. 19).

[45] Isaac Y. Tian, Michael C. Wong, Samantha Kennedy, Nisa N. Kelly, Yong E. Liu, Andrea K. Garber, Steven B. Heymsfield, Brian Curless, and John A. Shepherd. «A device-agnostic shape model for automated body composition estimates from 3D optical scans». In: *Medical Physics* 49.10 (2022), pp. 6395–6409 (cit. on p. 19).

[46] Matthew Loper, Naureen Mahmood, Javier Romero, Gerard Pons-Moll, and Michael J. Black. «SMPL: A Skinned Multi-Person Linear Model». In: *ACM Transactions on Graphics (TOG)* 34.6 (2015), 248:1–248:16 (cit. on p. 23).

[47] *Measurements & Landmarks Definitions v3.0*. Size Stream, LLC. 2022 (cit. on p. 24).

[48] F. I. Katch and W. D. McArdle. «Validity of body composition prediction equations for college men and women». In: *The American Journal of Clinical Nutrition* 28.2 (1975), pp. 105–109 (cit. on p. 24).

[49] Patrick S. Harty, Breck Sieglinger, Steven B. Heymsfield, John A. Shepherd, David Bruner, Matthew T. Stratton, and Grant M. Tinsley. «Novel body fat estimation using machine learning and 3-dimensional optical imaging». In: *European Journal of Clinical Nutrition* 74.5 (2020), pp. 842–845 (cit. on pp. 24, 28).

[50] Cassidy McCarthy, Grant M. Tinsley, Shengping Yang, Brian A. Irving, Michael C. Wong, Jonathan P. Bennett, John A. Shepherd, and Steven B. Heymsfield. «Smartphone prediction of skeletal muscle mass: model development and validation in adults». In: *The American Journal of Clinical Nutrition* 117.4 (2023), pp. 794–801 (cit. on p. 28).

[51] LLC Size Stream. *Medical and Wellness*. Accessed: 2025-05-15. 2025. URL: https://www.sizestream.com/solutions/medical-and-wellness (cit. on p. 29).

[52] Frank E. Grubbs. «Sample Criteria for Testing Outlying Observations». In: *Annals of Mathematical Statistics* 21.1 (1950), pp. 27–58 (cit. on p. 29).

[53] Gideon Schwarz. «Estimating the Dimension of a Model». In: *The Annals of Statistics* 6.2 (1978), pp. 461–464 (cit. on p. 47).

[54] Newcastle University. *Coefficient of determination (R-squared)*. Accessed: 2025-05-20. 2025. URL: https://www.ncl.ac.uk/webtemplate/ask-assets/external/maths-resources/statistics/regression-and-correlation/coefficient-of-determination-r-squared.html (cit. on pp. 48, 49).

[55] Deepak Kumar Sharma, Mayukh Chatterjee, Gurmehak Kaur, and Suchitra Vavilala. «Deep learning applications for disease diagnosis». In: *Deep Learning for Medical Applications with Unique Data*. Ed. by Deepak Gupta, Utku Kose, Ashish Khanna, and Valentina Emilia Balas. Academic Press, 2022, pp. 31–51 (cit. on p. 48).

[56] Nima Rezaei, Abbas Alimohammadi, and Abbas Maleki. «Introduction to Artificial Intelligence and Its Applications in the Petroleum Industry». In: *Applications of Artificial Intelligence Techniques in the Petroleum Industry*. Ed. by Abdolhossein Hemmati-Sarapardeh, Nima Rezaei, and Abbas Maleki. Elsevier, 2020, pp. 1–22 (cit. on p. 49).

[57] Massimiliano Grosso. *Principal Component Analysis (PCA) – GRICU PhD School 2021*. Lecture slides, GRICU PhD School – Digitalization Tools for the Chemical and Process Industries, March 12, 2021. Accessed: 2025-05-20. 2021 (cit. on p. 68).